A large strain hyperelastic viscoelastic-viscoplastic-damage constitutive model based on a multi-mechanism non-local damage continuum for amorphous glassy polymers

V.-D. Nguyen[a], F. Lani[b], T. Pardoen[b], X. P. Morelle[b], L. Noels[a,*]

[a]Computational & Multiscale Mechanical of Materials (CM3),
Department of Aerospace and Mechanical Engineering,
University of Liège,
Quartier Polytech 1, Allée de la Découverte 9, B-4000 Liège, Belgium
[b] Materials and Process Engineering (IMAP),
Institute of Mechanics, Materials and Civil Engineering,
Université catholique de Louvain,
Place Sainte Barbe 2, B-1348 Louvain-la-Neuve, Belgium

Abstract

A large strain hyperelastic phenomenological constitutive model is proposed to model the highly nonlinear, rate-dependent mechanical behavior of amorphous glassy polymers under isothermal conditions. A corotational formulation is used through the total Lagrange formalism. At small strains, the viscoelastic behavior is captured using the generalized Maxwell model. At large strains beyond a viscoelastic limit characterized by a pressure-sensitive yield function, which is extended from the Drucker-Prager one, a viscoplastic region follows. The viscoplastic flow is governed by a non-associated Perzyna-type flow rule incorporating this pressure-sensitive yield function and a quadratic flow potential in order to capture the volumetric deformation during the plastic process. The stress reduction phenomena arising from the post-peak plateau and during the failure stage are considered in the context of a continuum damage mechanics approach. The post-peak softening is modeled by an internal scalar, so-called softening variable, whose evolution is governed by a saturation law. When the softening variable is saturated, the rehardening stage is naturally obtained since the isotropic and kinematic hardening phenomena are still developing. Beyond the onset of failure characterized by a pressure-sensitive failure criterion, the damage process leading to the total failure is controlled by a second internal scalar, so-called failure variable. The final failure occurs when the failure variable reaches its critical value. To avoid the loss of solution uniqueness when dealing with the continuum damage mechanics formalism, a non-local implicit gradient formulation is used for both the softening and failure variables, leading to a multi-mechanism non-local damage continuum. The pressure sensitivity considered in both the yield and failure conditions allows for the distinction under compression and tension loading conditions. It is shown through experimental comparisons that the proposed constitutive model has the ability to capture the complex behavior of amorphous glassy polymers, including their failure.

Keywords: Glassy polymers, Large strain, Hyperelastic, Viscoelastic, Viscoplastic, Non-local damage, FEM

1. Introduction

Amorphous glassy polymers are widely used in combination with different types of fibers to manufacture fiber reinforced polymers (FRPs) for applications in a wide range of industrial components. Due to the increasing interest in FRPs, accurate constitutive representations of their constituents are more and more required to accurately capture the mechanical behavior through multi-scale analyses. By considering proper constitutive model for each constituent of composite materials, a computational micro-mechanics approach can be achieved to link up the FRPs behavior to not only constituent behaviors but also to the constituent arrangements as well as the constituent interactions (Canal et al., 2009; Melro et al., 2013, *e.g.*).
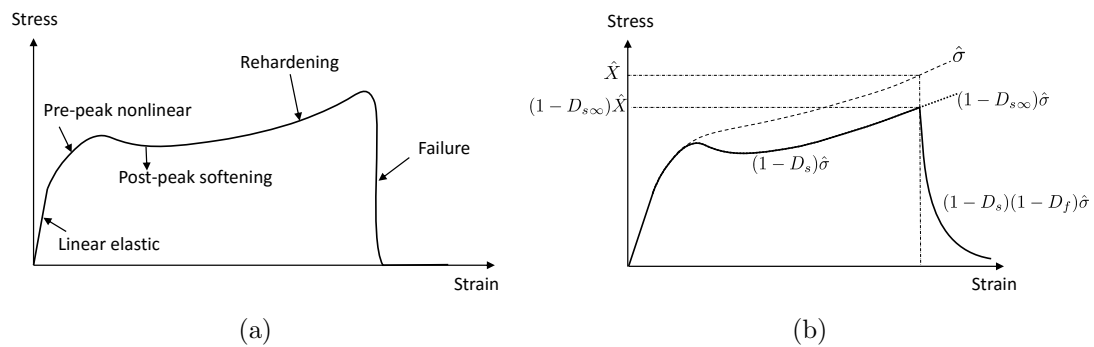
Figure 1: Typical stress-strain curve of amorphous glassy polymers at a constant given engineering strain rate: (a) multiple stages and (b) modeling strategy.

In general, the mechanical behavior of amorphous glassy polymers depends on the strain rate, hydrostatic pressure and temperature, as demonstrated through numerous experimental tests (Boyce et al., 1994; Lesser and Kody, 1997; Buckley et al., 2001; Fiedler et al., 2001; Chen et al., 2002; Hine et al., 2005; Mulliken and Boyce, 2006; Morelle et al., 2015). A typical stress-strain behavior for this kind of materials under uniaxial monotonic loading conditions is sketched out in Fig. 1a, in which the whole stress-strain curve can be divided into multiple stages. After an elastic stage at small strains, a nonlinear stage continues until reaching a peak stress, where large molecular movements can take place. After this peak value, the stress tends to decrease with increasing deformation. This effect is called softening. The physical origin of softening is still subject to debate but seems related to the kinetics of initiation, growth, and coalescence of shear transformation zones, which translate into the micro-shear banding as a true material feature (Morelle, 2015). At large strains, when the softening is saturated, a rehardening stage takes place until failure is

*Corresponding author, Phone: +32 4 366 48 26, Fax: +32 4 366 95 05

Email addresses: vandung.nguyen@ulg.ac.be (V.-D. Nguyen), frederic.lani@uclouvain.be (F. Lani), thomas.pardoen@uclouvain.be (T. Pardoen), xavier.morelle@uclouvain.be (X. P. Morelle), L.Noels@ulg.ac.be (L. Noels)

attained. The hardening phenomenon in glassy polymers has been interpreted using the analogy of an entropic spring (the three-dimensional polymer network), of which the non-linear stiffness depends notably either on the density of entanglements for thermoplastics (Boyce et al., 1988; Wu and van der Giessen, 1995; Tervoort et al., 1997) or the density of cross-links for thermosets. The compressive behavior differs from the tensile one as a result of the pressure-dependent yielding of polymers. Larger compressive peak stresses, failure stresses, and failure strains are normally observed in comparison to the tensile case at the same strain rate. The full range behavior shown in Fig. 1a is observed with epoxy resins under compressive loading, while under tensile loading the fracture of epoxy resin can occur prematurely before reaching the peak stress (Fiedler et al., 2001; Morelle et al., 2015), so the softening and rehardening phenomena are not always observed. In the case of a ductile, thermoplastic polymer (e.g. polycarbonate), this full range behavior appears in compression, tension, and shear loading conditions (Boyce et al., 1994). At small strain levels, the stiffness increases with the strain rates. A viscoelastic contribution should be taken into account at this stage. At higher strain levels, the non-linearity is enhanced with the presence of plasticity. The stress-strain response exhibits a strong strain rate dependence in the plastic regime. The material microstructure always involves internal defects at nano- and micro-scale. Moreover, the material microstructure can be modified under various loading conditions with the presence of some irreversible phenomena such as cavitation, and chain scission *etc.*, leading to a significant amount of micro-voids and micro-cracks. These pre-existing and arising defects can then contribute to the stress decrease in the softening stage and play an important role on the initiation of the failure stage. A couple viscoelastic-viscoplastic-damage constitutive model in the large strain framework is thus necessary in order to capture the entire range of stress-strain responses at various strain rates of these materials.

The rate dependent behavior of polymers in general can be modeled using a viscoelastic constitutive law. Some available viscoelastic models can be used as the generalized Maxwell model (Reese and Govindjee, 1998; Buhan and Frey, 2011), generalized Kelvin model (Zhang and Moore, 1997), fractional model (Schiessel et al., 1995), or Schapery model (Haj-Ali and Muliana, 2004). In these models, a network of multiple springs and dashpots is considered. The rate effect is modeled by a Newtonian fluid flow governing each dashpot. Although these models can be extended to the finite strain regime and consider non-linear Newtonian fluid flows for the dashpots, a proper viscoelastic constitutive model cannot capture the complex behavior of amorphous glassy polymers, which combines different complex mechanisms, such as plasticity, softening, failure ingredients, *etc.* This motivates the use of a more complex constitutive model. For this purpose many viscoplastic models have been proposed to predict the rate dependent behavior of polymers. On the one hand, the physically-based constitutive models have been proposed, see *e.g.* some physically-based models proposed by Boyce et al. (1988); Arruda et al. (1995); Tervoort et al. (1997); Govaert et al. (2000). Although these models can capture the complex behavior of polymers in the glassy state, the experimental calibration of their constitutive parameters can be complex. On the other hand, the phenomenological-based

constitutive models have been developed and sometimes provide an easier modeling approach. Most of them were initially used for metals and then extended to polymers. In this category, the Perzyna viscoplasticity theory (Perzyna, 1971) can be used to model the rate-dependent behavior of polymers as demonstrated by Van Der Sluis et al. (2001); Kim and Muliana (2010); Abu Al-Rub et al. (2015); the viscoplastic theory based on the overstress (VBO) concept (Krempl et al., 1986) can be considered for polymers as shown by Colak (2005); the Bodner and Partom viscoplastic model (Bodner and Partom, 1975) can be applied to polymers as also shown by Frank and Brockman (2001); Zaïri et al. (2008). The complex behavior of polymers can thus be captured using a viscoelastic-viscoplastic constitutive model with a robust integration algorithm to be implemented in finite element codes (Miled et al., 2011) by combining a viscoelastic constitutive model with a phenomenological-based viscoplastic one. Additionally, to model the material degradation when dealing with the fracture behavior of polymers, a viscoelastic-viscoplastic-damage constitutive model can be used (Abu Al-Rub et al., 2015; Zaïri et al., 2008; Krairi and Doghri, 2014). However, the complex mechanical behavior of amorphous glassy polymers exhibiting multiple stages coupled with the compression-tension asymmetry in both yielding and failure stages were not considered. The failure of amorphous glassy polymers can be studied with a physically-based constitutive model coupled with a crazing model as considered in Chowdhury et al. (2008a,b).

When dealing with softening phenomena, a continuum damage mechanics (CDM) approach can be used (Lemaitre and Chaboche, 1994; Kachanov, 2013). The material softening is modeled by a set of internal variables (so-called damage variables) in order to capture the local stress reduction. Beyond the onset of softening, the deformation tends to localize into a narrow zone. If a standard continuum is considered when strain localization happens, its underlying local action assumption, in which the stress state at a material point depends only on the deformation state at that point, leads to the loss of solution uniqueness. Consequently, the boundary value problem becomes ill-posed. The numerical solution obtained from the finite element method using the standard continuum differs with the mesh size and the mesh direction without convergence. Accordingly, the numerical solution becomes physically meaningless. This problem is not purely numerical since the mesh dependence is the direct consequence of ill-posedness of the underlying mathematical problem, *i.e.* the boundary value problem loses ellipticity in statics or hyperbolicity in dynamics (Engelen et al., 2003). Many non-local models have been proposed not only to address this numerical deficiency, but also to represent a physical behavior, see *e.g.* the overview by Bazant and Jirásek (2002) and its references. The ill-posed nature of the boundary value problem can be removed by incorporating an intrinsic length allowing interactions between neighboring material points. The physical meaning of such a length was studied for instance by Stölken and Evans (1998); Geers et al. (1999); Shu and Barlow (2000). Because a real material always possesses a complex microstructure, the material heterogeneity and true material failure mechanisms lead to local spatial variations of material properties. In the case of polymers, it was shown that crazing occurs at regular interval motivating the introduction of a length scale (Selke,

2016). Therefore, a non-local constitutive description needs to be considered since interactions between neighboring material points cannot be neglected. In this work, the non-local implicit formulation pioneered by Peerlings et al. (1996) is adopted as it can be easily integrated into a standard finite element formulation.

The main goal of this work is to develop a phenomenological viscoelastic-viscoplastic-damage constitutive model which has the ability to incorporate the viscoelasticity, viscoplasticity, softening, rehardening, and tension-compression asymmetry in both yielding and fracture processes with the following novelties:

- A large strain hyperelastic viscoelastic-viscoplastic-damage constitutive model able to capture not only multi-stage but also the compression-tension asymmetry in both yielding and failure in amorphous glassy polymers;

- A new power-enhanced yield condition generalized from the classical Drucker-Prager yield function;

- Multi-mechanism non-local damage continuum with a implicit gradient-enhanced formulation applied to multiple softening variables, in order to cover the problem of the loss of solution uniqueness when dealing with the strain softening phenomena;

- Identification of the constitutive parameters for the highly cross-linked RTM6 epoxy resin and validation by comparison with experimental tests under various constant engineering strain rates.

This coupled constitutive model is implemented in the hyperelastic large strain framework in a corotational formulation with the total Lagrange formalism, which was shown to be easily implemented in finite element codes (Eterovic and Bathe, 1990; Cuitino and Ortiz, 1992). The modeling strategy involves the following elements:

- At small strains, a viscoelastic behavior is assumed. The viscoelastic constitutive model is extended from the linear generalized Maxwell model. The rheological topology contains multiple spring-dashpot elements. Bi-logarithmic potential functions are considered in the springs and quadratic dissipation functions are considered in the dashpots. The total viscoelastic potential is then evaluated and the Kirchhoff stress expressed in the viscoelastic corotational space (so-called corotational Kirchhoff stress) is derived from this viscoelastic potential through its energetically conjugated measure.

- The viscoplastic threshold is defined using a pressure-sensitive yield condition upon which a viscoplastic flow takes place. In this work, a generalized version of the Drucker-Prager yield function is used with a power-enhancement on the octahedral term. The viscoplastic flow rule follows the Perzyna viscoplastic theory (Perzyna, 1971) incorporating this extended pressure-sensitive Drucker-Prager yield function with a pressure-sensitive plastic flow potential. In order to accurately predict the Poisson effect during the plastic flow, a non-associated flow rule is used. The choice of the non-associated flow rule allows predicting accurately the plastic Poisson effect using a plastic flow potential different from the yield

function. In this work, a quadratic flow potential is considered to correctly capture the volumetric deformation during the plastic process with a constant plastic Poisson ratio (Melro et al., 2013). Both isotropic and kinematic hardening phenomena are considered to capture the pre-peak non-linearity and rehardening stages.

- By combining the viscoelastic model with the Perzyna viscoplastic flow, a coupled viscoelastic-viscoplastic constitutive law without softening is obtained. In this work, the stress decrease in the softening stage is considered using the continuum damage mechanics (CDM) (Lemaitre and Chaboche, 1994; Kachanov, 2013), on which the softening behavior is modeled using a scalar variable, so-called softening variable, which is governed by a saturated law. After this stage, the rehardening sets in as the kinematic and isotropic hardening phenomena are still developing.

- The onset of the failure stage is predicted using a pressure-sensitive failure condition, which allows capturing distinct compression and tensile failure behaviors. Under the assumption that the failure occurrence is progressive, the failure stage is modeled in the context of the CDM by a second internal variable, so-called failure variable. Its value ranges from 0 at the failure onset to 1, which corresponds to final failure.

- A typical issue of the local CDM is the problem of loss of solution uniqueness when the softening occurs. This problem can be avoided using a non-local implicit formulation (Peerlings et al., 1996). In this work, two separated softening sources are considered, so that this remedy should be applied to both softening and failure variables. This requirement leads to consider a multi-mechanism non-local damage continuum, which allows an arbitrary number of softening variables to be combined; the particular case with two variables being easily deduced.

The paper is organized as follows. The generalities of the multi-mechanism non-local damage continuum are first presented in Section 2. The viscoelastic-viscoplastic-damage constitutive law is presented in Section 3, where the related theoretical aspects of viscoelastic, viscoplastic, and softening ingredients are detailed. The material parameters identification using experimental results of the RTM6 epoxy resin are discussed in Section 4. The numerical study on a notched sample is provided in Section 5 in order to demonstrate the mesh objectivity under damage propagation and localization. Finally, the experimental validation is reported in Section 6 in order to assess the identified constitutive parameters.

2. Non-local continuum damage mechanics

Let us consider a body B, whose reference configuration is B_0 and whose reference boundary is ∂B_0, subjected to a volumetric force $\mathbf{B}_0$. The boundary ∂B_0 can be divided into two distinct parts: the Dirichlet boundary part $\partial_D B_0$, where the displacement is prescribed to $\mathbf{u}_0$; and the Neumann boundary part $\partial_N B_0$,

where the surface traction is prescribed to $\mathbf{T}_0$. These two parts satisfy $\partial_D B_0 \cup \partial_N B_0 = \partial B_0$ and $\partial_D B_0 \cap \partial_N B_0 = \emptyset$. The equilibrium equations over the body B_0 under the quasi-static loading read

$$\mathbf{P} \cdot \boldsymbol{\nabla}_0 + \mathbf{B}_0 = \mathbf{0} \qquad \text{on } B_0, \tag{1}$$

$$\mathbf{u} = \mathbf{u}_0 \qquad \text{on } \partial_D B_0, \text{ and} \tag{2}$$

$$\mathbf{P} \cdot \mathbf{N} = \mathbf{T}_0 \qquad \text{on } \partial_N B_0, \tag{3}$$

where $\mathbf{P}$ is the first Piola-Kirchoff stress tensor and where $\mathbf{N}$ is the unit outward normal to ∂B_0 in the reference configuration. This problem statement is completed by a material constitutive law. In all generalities, this material constitutive law can be written as

$$\mathbf{P} = \mathbf{P}\left(\mathbf{F}(t); \mathbf{Z}(\tau), \tau \in [0 \ t]\right), \tag{4}$$

where $\mathbf{F}$ is the deformation gradient tensor and where $\mathbf{Z}$ is a vector that contains all internal variables in order to model history and path-dependent processes.

In this work, the softening phenomena are addressed in the context of the continuum damage mechanics (CDM) (Lemaitre and Chaboche, 1994; Kachanov, 2013). Basically, in the CDM, the material degradation is captured by an internal scalar D, so-called isotropic softening variable. The value of D varies from 0 for an intact material to 1 when the total failure occurs. Under the assumption that the strain measures in the current configuration and its undamaged representation are equivalent (Lemaitre, 1985), the first Piola-Kirchhoff stress is given by

$$\mathbf{P} = (1 - D)\hat{\mathbf{P}}, \tag{5}$$

where $\hat{\mathbf{P}}$, so-called the effective first Piola-Kirchhoff stress tensor, denotes the first Piola-Kirchhoff stress tensor in the undamaged representation. The required constitutive model (4) is then specified through the evolution of the softening variable D

$$\dot{D} = \mathfrak{D}\left(D, \mathbf{F}(t); \mathbf{Z}(\tau), \tau \in [0 \ t]\right), \tag{6}$$

and of the constitutive behavior of the respective undamaged material, which is expressed as

$$\hat{\mathbf{P}} = \hat{\mathbf{P}}\left(\mathbf{F}(t); \mathbf{Z}(\tau), \tau \in [0 \ t]\right). \tag{7}$$

A typical stress-strain curve $\sigma = \sigma(\varepsilon)$ of an amorphous glassy polymer exhibits multiple stages: elastic, pre-peak non-linearity, post-peak softening, rehardening, and failure, see Fig. 1a. The modeling strategy to capture these ingredients is schematically shown for the 1-dimensional case in Fig. 1b. From the effective stress-strain curve $\hat{\sigma} = \hat{\sigma}(\varepsilon)$, the softening stage is modeled using a softening variable denoted by D_s. The evolution of D_s obeys a saturation law, and tends to $D_{s\infty}$ when strains increase. When D_s reaches its

saturation value, the rehardening stage sets in since the hardening of the undamaged part is still developing. As a result, the evolution of D_s does not lead to the material failure. Therefore the onset of the failure stage is assessed by a failure criterion. After the onset of failure, the stress decrease is modeled using an internal variable, so-called failure variable, which is denoted by D_f. The value of D_f ranges from 0 at the onset of failure to 1, when final failure occurs. Thus, in order to capture the multi-stage behavior of amorphous glassy polymers, two distinct softening variables (D_s and D_f) are used so that Eq. (5) is rewritten as

$$\mathbf{P} = (1 - D_s)(1 - D_f)\hat{\mathbf{P}}\,. \tag{8}$$

By referring to Eq. (5), the softening variable D can be expressed by

$$D = 1 - (1 - D_s)(1 - D_f) = D_s + D_f - D_s D_f\,. \tag{9}$$

The constitutive relation (4) is now defined by the evolution of D_s and of D_f as

$$\dot{D}_{f,s} = \mathfrak{D}_{f,s}\left(D_{f,s}, \mathbf{F}(t); \mathbf{Z}(\tau), \tau \in [0\ t]\right)\,, \tag{10}$$

and by the constitutive behavior of the undamaged material, which is still specified by Eq. (7).

Following Eqs. (10), the actual values of D_s and of D_f at each material point depend on the actual strain and the strain history at that point, so that the relying modeling strategy is locally described. An important issue of a local CDM is the loss of solution uniqueness when strain softening occurs. The strain softening leads to ill-posed boundary value problem, pathological localization, and mesh dependent numerical solutions. These problems can be avoided using the non-local implicit approach pioneered by Peerlings et al. (1996). In this non-local model, some internal variables φ, which can be the strain, the accumulative plastic strain, a damage indicator, *etc.*, are considered in a weighted average form, so-called non-local variables $\bar{\varphi}$, over a characteristic volume V_c at the material point $\mathbf{X}$. This allows taking into account the influence of the neighboring material points. One has

$$\bar{\varphi}(\mathbf{X}) = \frac{1}{V_c} \int_{V_c} \varphi(\mathbf{Y})\, \theta(\mathbf{r})\, d\Omega\,, \tag{11}$$

where $\mathbf{r} = \mathbf{Y} - \mathbf{X}$ is the radius vector, where $\mathbf{Y}$ denotes the position of a point inside the characteristic volume V_c in the material coordinate, and where $\theta(\mathbf{r})$ is the weight function, which reflects the influence of neighboring material points and satisfies

$$\frac{1}{V_c} \int_{V_c} \theta\, d\Omega = 1\,. \tag{12}$$

After some mathematical manipulations, Eq. (11) leads to a Helmholtz-type equation (Peerlings et al., 1996, 2001)

$$\bar{\varphi} - l^2 \Delta_0 \bar{\varphi} = \varphi\,. \tag{13}$$

8

The non-local variable $\bar{\varphi}$ is given by an implicit form from its local counterpart leading to a new boundary value problem. In Eq. (13), l is the characteristic size of the material. This non-local variable $\bar{\varphi}$ is associated to the softening variable D, whose evolution depends on the evolution of the non-local variable $\bar{\varphi}$ via a general rate form

$$\dot{D} = \mathfrak{D} \left(D, \mathbf{F}(t), \chi(t); \mathbf{Z}(\tau), \tau \in [0 \; t] \right) \dot{\chi} , \tag{14}$$

where $\mathbf{Z}$ is a vector containing the undamaged material internal variables and where χ is a monotonically increasing non-local variable

$$\chi(t) = \max \left[\chi_0, \bar{\varphi}(\tau) \, ; \, 0 \leq \tau \leq t \, \right] . \tag{15}$$

In the last equation, χ_0 is the onset of the damage evolution. The purpose of Eq. (15) is to define the onset and the irreversibility of the damaging process.

In this work, the softening and the failure variables are considered independently. The implicit non-local formulation described in Eq. (13) is applied not only to D_s but also to D_f in order to avoid the problem of loss of solution uniqueness, which can occur for both the softening and failure stages. This results in an implicit non-local formulation for the softening variable (with a subscript s)

$$\bar{\varphi}_s - l_s^2 \Delta_0 \bar{\varphi}_s = \varphi_s , \tag{16}$$

$$\dot{D}_s = \mathfrak{D}_s \left(D_s, \mathbf{F}(t), \chi_s(t); \mathbf{Z}(\tau), \tau \in [0 \; t] \right) \dot{\chi}_s , \text{ and} \tag{17}$$

$$\chi_s(t) = \max \left[\chi_{s0}, \bar{\varphi}_s(\tau) \, ; \, 0 \leq \tau \leq t \, \right] , \tag{18}$$

and in an implicit non-local formulation for the failure variable (with a subscript f)

$$\bar{\varphi}_f - l_f^2 \Delta_0 \bar{\varphi}_f = \varphi_f , \tag{19}$$

$$\dot{D}_f = \mathfrak{D}_f \left(D_f, \mathbf{F}(t), \chi_f(t); \mathbf{Z}(\tau), \tau \in [0 \; t] \right) \dot{\chi}_f , \text{ and} \tag{20}$$

$$\chi_f(t) = \max \left[\chi_{f0}, \bar{\varphi}_f(\tau) \, ; \, 0 \leq \tau \leq t \, \right] . \tag{21}$$

In Eqs. (16, 19), l_s and l_f are the characteristic sizes of the softening and of the failure phenomena, respectively. The non-local implicit formulation expressed in Eqs. (16, 19) is completed by natural boundary conditions (Peerlings et al., 1996)

$$\boldsymbol{\nabla}_0 \bar{\varphi}_k \cdot \mathbf{N} = 0 \text{ on } \partial B_0 \text{ with } k = s, f . \tag{22}$$

The selection of the local variables for the softening and failure stages as well as the expression of $\mathfrak{D}_s$ and $\mathfrak{D}_f$ are discussed in Section 3.2 after having described the undamaged material law in Eq. (7) in Section 3.1. The weak form and the finite element resolution of the strong form stated in Eqs. (1, 16, 19) with the boundary conditions (2, 3, 22) are detailed in Appendix A.

3. Constitutive model

This section presents the details of the constitutive model able to capture the multi-stage behavior of glassy amorphous polymers. By using non-local formulations, the evolution of softening variables is uncoupled from the constitutive relation of the undamaged part. First, the viscoelastic-viscoplastic constitutive law specified in Eq. (7) is detailed. Then the local variables φ_s and φ_f for the softening and failure stages are respectively defined. Next the evolution laws (17) and (20) of the softening variables respected with their respective non-local variables are provided. Finally, the constitutive model and the relevant material parameters are summarized.

3.1. Viscoelastic-viscoplastic constitutive model

3.1.1. Kinematics

At time t, the position $\mathbf{x}$ of the material particle in the current configuration B is a 2-point mapping of the position $\mathbf{X}$ of this material particle in the reference configuration B_0, at time $t = 0$. This 2-point mapping is expressed under the form $\mathbf{x} = \mathbf{x}(\mathbf{X}, t)$. The deformation gradient is then defined by

$$\mathbf{F} = \frac{\partial \mathbf{x}}{\partial \mathbf{X}}, \tag{23}$$

with its Jacobian $J = \det \mathbf{F} > 0$.

Following the standard multiplicative decomposition used in viscoelastic-viscoplastic materials, the deformation gradient $\mathbf{F}$ is decomposed into a viscoelastic and a viscoplastic parts (Moran et al., 1990) as follows

$$\mathbf{F} = \mathbf{F}^{ve} \cdot \mathbf{F}^{vp}, \tag{24}$$

where $\mathbf{F}^{ve}$ and $\mathbf{F}^{vp}$ represent respectively the viscoelastic and viscoplastic deformation gradients. The right Cauchy strain tensors are given by

$$\mathbf{C} = \mathbf{F}^T \cdot \mathbf{F}, \quad \mathbf{C}^{ve} = \mathbf{F}^{veT} \cdot \mathbf{F}^{ve}, \quad \mathbf{C} = \mathbf{F}^{vpT} \cdot \mathbf{C}^{ve} \cdot \mathbf{F}^{vp}. \tag{25}$$

From the deformation gradient decomposition, the viscoplastic spatial gradient of velocity is defined by

$$\mathbf{L}^{vp} = \dot{\mathbf{F}}^{vp} \cdot \mathbf{F}^{vp-1}. \tag{26}$$

$\mathbf{L}^{vp}$ can be decomposed into its symmetric part $\mathbf{D}^{vp}$, so-called viscoplastic strain rate tensor and its anti-symmetric part $\mathbf{W}^{vp}$, so-called viscoplastic spin tensor, such that

$$\mathbf{L}^{vp} = \mathbf{D}^{vp} + \mathbf{W}^{vp}, \mathbf{L}^{vp} = \frac{1}{2}\left(\mathbf{L}^{vp} + \mathbf{L}^{vpT}\right), \text{ and } \mathbf{W}^{vp} = \frac{1}{2}\left(\mathbf{L}^{vp} - \mathbf{L}^{vpT}\right). \tag{27}$$

By assuming an irrotational viscoplastic flow, $\mathbf{W}^{vp} = \mathbf{0}$, and Eq. (27) becomes

$$\mathbf{D}^{vp} = \mathbf{L}^{vp} = \dot{\mathbf{F}}^{vp} \cdot \mathbf{F}^{vp-1}, \tag{28}$$

from which the plastic evolution can be determined as

$$\dot{\mathbf{F}}^{vp} = \mathbf{D}^{vp} \cdot \mathbf{F}^{vp} \,, \tag{29}$$

with $\mathbf{D}^{vp}$ specified through the viscoplastic flow rule, which is detailed later.

3.1.2. Logarithmic strain and stress measures

The strain measures are defined using the logarithmic operator. The total strain and viscoelastic part are respectively defined by

$$\mathbf{E} = \frac{1}{2} \ln \mathbf{C} \,, \ \text{and} \ \mathbf{E}^{ve} = \frac{1}{2} \ln \mathbf{C}^{ve} \,. \tag{30}$$

The material model is based on an hyperelastic formulation assuming the existence of an elastic potential $\Psi(\mathbf{E}^{ve})$, which depends only on the viscoelastic strain part. The conjugated stress measures are defined from this potential as

$$\dot{\Psi} = \hat{\boldsymbol{\kappa}} : \mathbf{L}^{ve} = \hat{\boldsymbol{\tau}} : \dot{\mathbf{E}}^{ve} \,, \tag{31}$$

where $\hat{\boldsymbol{\kappa}}$ is the effective Kirchhoff stress and where $\hat{\boldsymbol{\tau}}$ is the effective stress measure conjugated to the logarithmic strain $\mathbf{E}^{ve}$. From Eq. (31), one has

$$\hat{\boldsymbol{\kappa}} = 2\mathbf{F}^{ve} \cdot \frac{\partial \Psi}{\partial \mathbf{C}^{ve}} \cdot \mathbf{F}^{veT} = \mathbf{F}^{ve-T} \cdot \hat{\boldsymbol{\tau}} \cdot \mathbf{F}^{veT} \,. \tag{32}$$

As demonstrated by Eterovic and Bathe (1990), the stress measure conjugated to the viscoelastic logarithmic strain (denoted by $\hat{\boldsymbol{\tau}}$) corresponds to the Kirchhoff stress (denoted by $\hat{\boldsymbol{\kappa}}$) expressed in the viscoelastic corotational space. The stress measure $\hat{\boldsymbol{\tau}}$ is then called the effective corotational Kirchhoff stress.

Finally, the effective first Piola-Kirchhoff stress $\hat{\mathbf{P}}$, which is conjugated to the deformation gradient $\mathbf{F}$, is estimated from the Kirchhoff stress and the deformation gradient by the relation

$$\hat{\mathbf{P}} = \hat{\boldsymbol{\kappa}} \cdot \mathbf{F}^{-T} = 2\mathbf{F}^{ve} \cdot \frac{\partial \Psi}{\partial \mathbf{C}^{ve}} \cdot \mathbf{F}^{vp-T} = \mathbf{F}^{ve-T} \cdot \hat{\boldsymbol{\tau}} \cdot \mathbf{F}^{vp-T} \,. \tag{33}$$

3.1.3. Viscoelastic part

The viscoelastic constitutive relation is based on an hyperelastic formulation under the assumption that an elastic potential function exists. The viscoelastic behavior is modeled by the generalized Maxwell model containing $N + 1$ springs and N dashpots as shown in Fig. 2. This allows defining the total viscoelastic potential (Simo, 1987) from potential and dissipation functions on each branch as

$$\Psi \left(\mathbf{E}^{ve}; \mathbf{q}_1, ..., \mathbf{q}_N \right) = \Psi_\infty \left(\mathbf{E}^{ve} \right) + \sum_{i=1}^{N} \left[\Psi_i \left(\mathbf{E}^{ve} \right) + \Upsilon_i \left(\mathbf{E}^{ve}; \mathbf{q}_i \right) \right] \,, \tag{34}$$
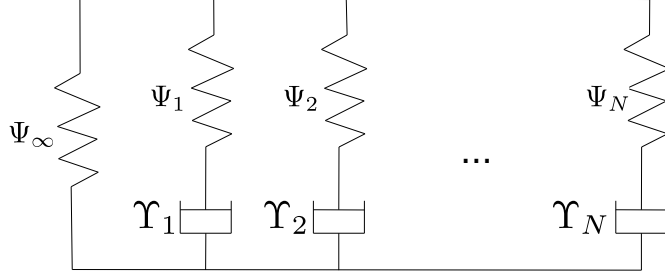
Figure 2: Springs/dashpots network of the generalized Maxwell model.

where Ψ_i with $i = \infty, 1, ..., N$ are the elastic potentials of the springs, where Υ_i with $i = 1, ..., N$ are the dissipating functions of the dashpots, and where $\mathbf{q}_i$ with $i = 1, ..., N$ are internal variables governing the viscoelastic process. The bi-logarithmic potential function is used for the spring

$$\Psi_i(\mathbf{C}^{ve}) = \frac{K_i}{2} \ln^2 J^{ve} + G_i \left(\text{dev } \mathbf{E}^{ve}\right) : \left(\text{dev } \mathbf{E}^{ve}\right) \text{ with } i = \infty, 1, ..., N, \tag{35}$$

and the quadratic dissipating function is considered for the dashpot (Simo, 1987)

$$\Upsilon_i\left(\mathbf{E}^{ve}, \mathbf{q}_i\right) = -\mathbf{q}_i : \mathbf{E}^{ve} + \left[\frac{1}{18K_i}\left(\text{tr } \mathbf{q}_i\right)^2 + \frac{1}{4G_i}\text{dev } \mathbf{q}_i : \text{dev } \mathbf{q}_i\right] \text{ with } i = 1, ..., N. \tag{36}$$

In Eqs. (35, 36), K_i and G_i with $i = \infty, 1, ..., N$ are respectively the bulk and shear moduli of the materials. The viscoelastic effect is considered in both volumetric and deviatoric parts through the internal variables $\mathbf{q}_i$ with $i = 1, ..., N$. The evolution of $\mathbf{q}_i$ is characterized by a retardation action (Simo, 1987) as follows

$$\text{dev } \dot{\mathbf{q}}_i = \frac{2G_i}{g_i}\text{dev } \mathbf{E}^{ve} - \frac{1}{g_i}\text{dev } \mathbf{q}_i, \text{ and} \tag{37}$$

$$\text{tr } \dot{\mathbf{q}}_i = \frac{3K_i}{k_i}\text{tr } \mathbf{E}^{ve} - \frac{1}{k_i}\text{tr } \mathbf{q}_i, \tag{38}$$

where g_i and k_i are the retardation characteristic times for the deviatoric and volumetric parts, respectively.

From Eq. (34), the effective corotational Kirchhoff stress can be estimated by

$$\hat{\boldsymbol{\tau}} = \frac{\partial \Psi}{\partial \mathbf{E}^{ve}} = \hat{\boldsymbol{\tau}}_\infty^0 + \sum_{i=1}^{N}\left(\hat{\boldsymbol{\tau}}_i^0 - \mathbf{q}_i\right), \tag{39}$$

where

$$\hat{\boldsymbol{\tau}}_i^0 = \frac{\partial \Psi_i\left(\mathbf{E}^{ve}\right)}{\partial \mathbf{E}^{ve}} = K_i \text{tr } \mathbf{E}^{ve}\mathbf{I} + 2G_i\text{dev } \mathbf{E}^{ve} \text{ with } i = \infty, 1, ..., N. \tag{40}$$

The system of rate equations (37) and (38) leads the resolution of the $\mathbf{q}_i$ internal variable under simple convolution integrals

$$\text{dev } \mathbf{q}_i = \frac{2G_i}{g_i}\int_{-\infty}^{t}\exp\left(-\frac{t-s}{g_i}\right)\text{dev } \mathbf{E}^{ve}(s)\,ds, \text{ and} \tag{41}$$

$$\text{tr } \mathbf{q}_i = \frac{3K_i}{k_i}\int_{-\infty}^{t}\exp\left(-\frac{t-s}{k_i}\right)\text{tr } \mathbf{E}^{ve}(s)\,ds. \tag{42}$$

12

Substituting Eqs. (41, 42) into Eq. (39) leads to the solution of the effective corotational Kirchhoff stress

$$\text{dev}\,\hat{\boldsymbol{\tau}} \;=\; \int_{-\infty}^{t} 2G(t-s) : \frac{\mathrm{d}}{\mathrm{d}s}\text{dev}\,\mathbf{E}^{ve}(s)\,ds\,, \text{ and} \tag{43}$$

$$\hat{p} \;=\; \frac{1}{3}\text{tr}\,\hat{\boldsymbol{\tau}} = \int_{-\infty}^{t} K(t-s)\frac{\mathrm{d}}{\mathrm{d}s}\text{tr}\,\mathbf{E}^{ve}(s)\,ds\,, \tag{44}$$

where

$$G(t) = G_{\infty} + \sum_{i=1}^{N} G_i \exp\left(-\frac{t}{g_i}\right)\,, \text{ and } K(t) = K_{\infty} + \sum_{i=1}^{N} K_i \exp\left(-\frac{t}{k_i}\right)\,. \tag{45}$$

The effective corotational Kirchhoff stress is estimated from its deviatoric and volumetric parts by

$$\hat{\boldsymbol{\tau}} = \text{dev}\,\hat{\boldsymbol{\tau}} + \hat{p}\mathbf{I}\,. \tag{46}$$

The effective first Piola-Kirchhoff stress is thus estimated using Eq. (33) as

$$\hat{\mathbf{P}} = \mathbf{F}^{ve} \cdot (\hat{\boldsymbol{\tau}} : \mathcal{L}) \cdot \mathbf{F}^{vp-T}\,, \tag{47}$$

where

$$\mathcal{L} = \left.\frac{\partial \ln \mathbf{C}^{ve}}{\partial \mathbf{C}^{ve}}\right|_{\mathbf{C}^{ve}}\,. \tag{48}$$

Note that as the computation of the logarithmic operator involves approximations, its derivatives ought to account for those approximations; that explains the use of $\mathcal{L}$ instead of $\mathbf{C}^{ve-1}$, see the implementation in Appendix B.

3.1.4. Viscoplastic part

The viscoelastic region is limited by a pressure-sensitive yielding condition, which is detailed in this section. The yield function F is expressed in terms of the effective corotational Kirchhoff stress $\hat{\boldsymbol{\tau}}$ instead of the effective Kirchhoff stress $\hat{\boldsymbol{\kappa}}$. That is argued as the yield function is often expressed in terms of the stress invariants which are identical for $\hat{\boldsymbol{\tau}}$ and $\hat{\boldsymbol{\kappa}}$, while the numerical implementation with the corotational Kirchhoff stress can be easily performed thanks to the simple relation between the corotational Kirchhoff stress $\hat{\boldsymbol{\tau}}$ and the elastic logarithmic strain part $\mathbf{E}^{ve}$ in Eq. (46).

The viscoplastic behavior of amorphous glassy polymers is governed by a non-associated Perzyna-type viscoplastic flow rule (Perzyna, 1971), which can be expressed by the following relation

$$\mathbf{D}^{vp} = \frac{1}{\eta}\,\langle F\rangle^{\frac{1}{p}}\,\mathbf{Q}\,, \tag{49}$$

where $\mathbf{D}^{vp}$ is the visco-plastic strain rate as defined in Eq. (28), F is the yield function, η is the viscosity parameter, p is the rate sensitivity exponent, $\langle\bullet\rangle$ denotes the McAuley brackets defined by $\langle F\rangle = \frac{1}{2}\left(F + |F|\right)$, and where $\mathbf{Q}$ is the normal to the plastic flow potential

$$\mathbf{Q} = \frac{\partial P}{\partial \hat{\boldsymbol{\tau}}}\,. \tag{50}$$

13

In this last equation, P is the flow potential. In this work, the non-associate flow rule is assumed, $F \neq P$ in Eqs. (49, 50). The viscoplastic consistency parameter is defined from Eq. (49) as

$$\lambda = \frac{1}{\eta} \langle F \rangle^{\frac{1}{p}} , \tag{51}$$

from which, in the viscoplastic range, one can define a new yield condition

$$\bar{F} = F - (\eta \lambda)^p \leq 0 . \tag{52}$$

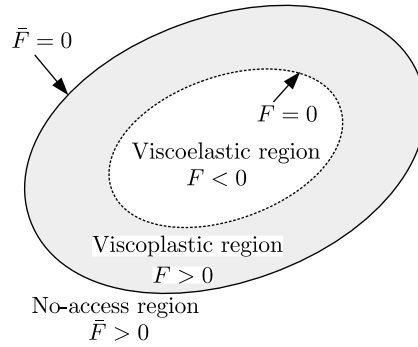The condition (52) is a generalized yield condition for rate-dependent materials.

Figure 3: Distinct regions considering in the viscoelastic-viscoplastic model.

The conceptual representation of the current viscoelastic-viscoplastic model is shown in Fig. 3. Below the plastic limit characterized by $F < 0$, the material obeys the viscoelastic behavior, in which both F and $\bar{F}$ are equivalent. When plasticity occurs, the yield surface is extended by a term depending on the strain rate. A generalized version of the Kuhn-Tucker condition is used, with

$$\lambda \bar{F} = 0 , \lambda \geq 0 , \text{ and } \bar{F} \leq 0 . \tag{53}$$

The rate-independent case can be simply recovered by constraining the viscosity parameter $\eta = 0$, which corresponds to no viscosity effect. In this formulation, the viscoelastic region always exists and is limited by the yield function at zero strain rate (denoted by F in this work). The details of the yield function and flow potential function are given in the following.

Yield function: In this work, a generalized version of the Drucker-Prager yield function is considered, so that the tension-compression asymmetry is employed. The yield function is expressed in terms of the combined stress tensor denoted by $\boldsymbol{\phi}$, which is defined by

$$\boldsymbol{\phi} = \hat{\boldsymbol{\tau}} - \mathbf{b} , \tag{54}$$

where $\mathbf{b}$ is the corotational backstress tensor. The Drucker-Prager yield function is generally expressed by a linear combination of the first and second invariants of the combined stress tensor, such as

$$F(\boldsymbol{\phi}) = a_2 \phi_e - a_1 \phi_p - a_0 , \tag{55}$$

14

where

$$\phi_p = \frac{1}{3}\mathrm{tr}\,\boldsymbol{\phi} \text{ and } \phi_e = \sqrt{\frac{3}{2}\mathrm{dev}\,\boldsymbol{\phi} : \mathrm{dev}\,\boldsymbol{\phi}}\,. \tag{56}$$

In this work, the Drucker-Prager yield function (55) is enhanced with an exponent on the octahedral term, yielding

$$F(\boldsymbol{\phi}) = a_2\,(\phi_e)^{\alpha} - a_1\phi_p - a_0\,, \tag{57}$$

where the three coefficients a_2, a_1, a_0 are functions of the equivalent plastic strain in order to model the evolution of the yield surface due to the isotropic hardening. Because of two stress invariants (pressure and von Mises equivalent stress), these three coefficients are determined from two yielding conditions at two distinct pressure states. Each yielding condition can be chosen either from simple loading cases (uniaxial tension, uniaxial compression, pure shear, pure pressure) or from a general loading case, in which the pressure and von Mises stress at the yielding condition can be derived. In this work, uniaxial compressive and uniaxial tensile yielding conditions are adopted but other cases can be easily derived. Under compressive and tensile uniaxial loading conditions, one has

$$\begin{cases} a_2\,(\sigma_c)^{\alpha} - a_1\frac{-\sigma_c}{3} - a_0 = 0 \\ a_2\,(\sigma_t)^{\alpha} - a_1\frac{\sigma_t}{3} - a_0 = 0 \end{cases}, \tag{58}$$

where σ_c and σ_t are the current compressive and tensile flow stresses, respectively. In this work, the compressive and tensile flow stresses are considered as being functions of the equivalent plastic strain, denoted by γ. The evolution of the equivalent plastic strain γ during plastic deformations is provided after defining the plastic flow potential in this section. In terms of the current compressive and tensile flow stresses (σ_c and σ_t), the homogeneous system of equations (58) results into

$$\begin{cases} a_1 = 3\frac{(\sigma_t)^{\alpha} - (\sigma_c)^{\alpha}}{\sigma_c + \sigma_t}a_2 \\ a_0 = \frac{(\sigma_t)^{\alpha}\sigma_c + (\sigma_c)^{\alpha}\sigma_t}{\sigma_c + \sigma_t}a_2 \end{cases}. \tag{59}$$

An arbitrary non-zero value of a_2 can be used as a normalization value of the yield function (57). By choosing $a_2 = \frac{1}{\sigma_c^{\alpha}}$ and defining the tension-compression flow asymmetry m by

$$m = \frac{\sigma_t}{\sigma_c}\,, \tag{60}$$

one finally has

$$a_2 = \frac{1}{\sigma_c^{\alpha}}\,,\ a_1 = 3\frac{m^{\alpha} - 1}{m + 1}\frac{1}{\sigma_c}\,,\ \text{and } a_0 = \frac{m^{\alpha} + m}{m + 1}\,. \tag{61}$$

The convexity of the yield function (57) implies that its Hessian, which is given by

$$\frac{\partial^2 F}{\partial\hat{\boldsymbol{\tau}}\partial\hat{\boldsymbol{\tau}}} = a_2\alpha\,(\phi_e)^{\alpha-1}\,\frac{\partial^2 \phi_e}{\partial\hat{\boldsymbol{\tau}}\partial\hat{\boldsymbol{\tau}}} + a_2\alpha\,(\alpha - 1)\,(\phi_e)^{\alpha-2}\,\frac{\partial\phi_e}{\partial\hat{\boldsymbol{\tau}}} \otimes \frac{\partial\phi_e}{\partial\hat{\boldsymbol{\tau}}}\,, \tag{62}$$

15

as the second derivative of the pressure term vanishes, remains positive semidefinite for all plastic states. The Hessian of the von Mises equivalent stress ($\frac{\partial^2 \phi_e}{\partial \hat{\tau} \partial \hat{\tau}}$) is positive semidefinite as demonstrated in Bigoni and Piccolroaz (2004). The dyadic tensor $\frac{\partial \phi_e}{\partial \hat{\tau}} \otimes \frac{\partial \phi_e}{\partial \hat{\tau}}$ is also positive semidefinite. As a result, the positive semidefinite condition of the Hessian following Eq. (62) is always satisfied when considering $\alpha \geq 1$ since the values of a_2 and of ϕ_e are always positive. In this work, the value of $\alpha \geq 1$ is used in order to ensure the convexity of the yield surface for all values of the equivalent plastic strain.

As the yield condition (57) is expressed in terms of the corotational Kirchhoff stress $\hat{\tau}$, the yield stresses σ_c and σ_t and backstress $\mathbf{b}$ are also Kirchhoff quantities in the viscoelastic corotational space, which differ from the Cauchy quantities by the deformation Jacobian. The use of σ_c and σ_t allows considering isotropic hardening effects, while the kinematic hardening one can be captured through the backstress $\mathbf{b}$.

In Eq. (57), an arbitrary value of the exponent α can be used leading to a new class of yield surfaces, so-called power yield surfaces. When $\alpha = 1$ this yield function (57) degenerates to the classical Drucker-Prager function and when $\alpha = 2$ it degenerates to the paraboloidal case as considered by Melro et al. (2013). Without considering the strain rate effects, the results with different values of α are presented in Fig. 4 and are compared to the experimental results. It shows that the proposed powered-enhanced yield function captures better the pressure-dependency of the experimental results, while the Drucker-Prager and the paraboloidal cases overestimate the results.
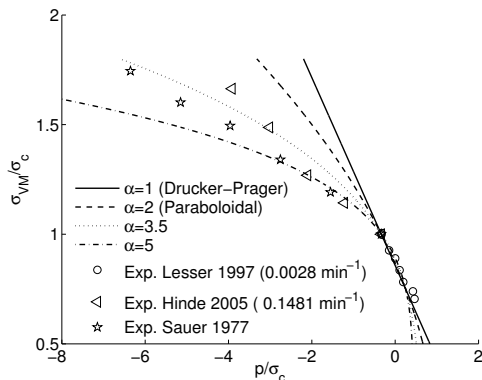

Figure 4: Power yield function (57) is depicted for different power values α, and with $m = 0.75$. The results are compared with the experimental results extracted from the works of Lesser and Kody (1997), of Hine et al. (2005), and of Sauer (1977) for epoxy resins. In this figure, σ_{VM} is the von Mises equivalent stress, p is the hydrostatic stress.

Flow potential: Because the viscoplastic behavior of the polymers is complex in general, a non-associated flow rule is often assumed (Melro et al., 2013; Abu Al-Rub et al., 2015; Vogler et al., 2013). Therefore, the evolution of the plastic flow is not determined by the gradient of the yield function (associated flow rule), but by the gradient of a plastic flow potential P. The choice of the non-associated flow rule allows correctly predicting the Poisson effect during the plastic process using suitable parameters of this

flow potential. In this work, a quadratic function is used as

$$P = \phi_e^2 + \beta \phi_p^2 \,, \tag{63}$$

where ϕ_e and ϕ_p are given in Eq. (56) and where β is a material parameter. The use of the quadratic flow potential allows capturing the volumetric plastic deformation with a constant plastic Poisson ratio (Melro et al., 2013)

$$\nu_p = \frac{9 - 2\beta}{18 + 2\beta} \,. \tag{64}$$

The plastic Poisson ratio ν_p is a material constant defining the value of β. The equivalent plastic deformation $\dot{\gamma}$ is defined from the viscoplastic rate tensor expressed in Eq. (49) by the following relation (Melro et al., 2013)

$$\dot{\gamma} = k\sqrt{\mathbf{D}^{vp} : \mathbf{D}^{vp}} \,, \tag{65}$$

where

$$k = \frac{1}{\sqrt{1 + 2\nu_p^2}} \,. \tag{66}$$

In case of an incompressible flow rule, $\nu_p = 0.5$, and the classical value of $k = \sqrt{\frac{2}{3}}$ is recovered.

Hardening effects: The kinematic hardening is modeled through the corotational backstress tensor $\mathbf{b}$. The evolution of backstress tensor $\mathbf{b}$ is specified by

$$\dot{\mathbf{b}} = k H_b(\gamma) \mathbf{D}^{vp} \text{ with } \mathbf{b}(\gamma = 0) = \mathbf{0} \,, \tag{67}$$

where k is given in Eq. (66), and where H_b is the kinematic hardening modulus, which depends on the equivalent plastic strain. In terms of equivalent values, Eq. (67) becomes

$$\dot{b}_e = H_b \dot{\gamma} \,, \text{ with } \dot{b}_e = \sqrt{\dot{\mathbf{b}} : \dot{\mathbf{b}}} \,. \tag{68}$$

The isotropic hardening is considered using distinctive compressive and tensile yield stresses, which can be independently introduced in the model as follows

$$\dot{\sigma}_c = H_c(\gamma)\dot{\gamma} \,, \text{ with } \sigma_c(\gamma = 0) = \sigma_c^0 \text{ and} \tag{69}$$

$$\dot{\sigma}_t = H_t(\gamma)\dot{\gamma} \,, \text{ with } \sigma_t(\gamma = 0) = \sigma_t^0 \,, \tag{70}$$

where H_c and H_t are the compressive and tensile isotropic hardening moduli, respectively.

All hardening moduli (including tensile isotropic, compressive isotropic, and kinematic) are defined as

functions of the equivalent plastic strain by the following general forms

$$H_t = \sum_{i=0}^{M_t} t_i \gamma^i + H_t^0 \exp\left(-K_t \gamma\right), \tag{71}$$

$$H_c = \sum_{i=0}^{M_c} c_i \gamma^i + H_c^0 \exp\left(-K_c \gamma\right), \text{ and} \tag{72}$$

$$H_b = \sum_{i=0}^{M_b} \beta_i \gamma^i + H_b^0 \exp\left(-K_b \gamma\right), \tag{73}$$

where M_t, M_c, M_b are the polynomial orders and where t_i with $i = 0, ..., M_t$, c_i with $i = 0, ..., M_c$, β_i with $i = 0, ..., M_b$, H_t^0, H_c^0, H_b^0, K_t, K_c and K_b are material parameters. In these equations, the polynomial terms are used to model the hardening, while the exponential terms are considered to capture the saturation state. The kinematic hardening modulus is mandatory to capture the Bauschinger effect upon unloading. The use of two independent yield stresses at two pressure states (here uni-axial compressive and tensile yield stresses) allows capturing the asymmetry in the compressive-tensile plastic flow behavior, which is present in glassy polymers as discussed by Poulain et al. (2014).

Viscoplastic extended yield condition: Using Eqs. (49, 50, 51, 63), Eq. (65) becomes

$$\dot{\gamma} = k\lambda\sqrt{6\phi_e^2 + \frac{4}{3}\beta^2\phi_p^2}. \tag{74}$$

Therefore, the viscoplastic extended yield function expressed in Eq. (52) is rewritten

$$\bar{F} = \left(\frac{\phi_e}{\sigma_c}\right)^\alpha - 3\frac{m^\alpha - 1}{m + 1}\frac{\phi_p}{\sigma_c} - \frac{m^\alpha + m}{m + 1} - \left(\frac{\eta\dot{\gamma}}{k\sqrt{6\phi_e^2 + \frac{4}{3}\beta^2\phi_p^2}}\right)^p \leq 0. \tag{75}$$

The rate dependency in the plastic region is taken into account with the presence of the plastic equivalent strain rate in the extended yield surface (75).

Considering a uniaxial test, one has at the plasticity onset $\phi_e = |\sigma|$, $\phi_p = \pm\frac{|\sigma|}{3}$, and $\sigma_c = \sigma_c^0$, where the notations $+$ and $-$ correspond to the tension and compression cases, respectively. The initial yield stress value with the strain effects is thus estimated from Eq. (75) by solving the equation

$$f^\alpha - \frac{m^\alpha - 1}{m + 1}(\pm f) - \frac{m^\alpha + m}{m + 1} - \left(\frac{z}{kf\sqrt{6 + \frac{4}{27}\beta^2}}\right)^p = 0, \tag{76}$$

where

$$f = \frac{|\sigma|}{\sigma_c^0} \text{ and } z = \frac{\eta\dot{\gamma}}{\sigma_c^0}. \tag{77}$$

The solution of Eq. (76) leads to the relationship $f = f(z)$, which describes the dependence of the initial yield stress on the plastic equivalent strain rate. This relation is depicted in Fig. 5 for different values of the yield exponent α and of the rate sensitivity exponent p, with $m = 0.75$ and $\beta = 0.3$. The increase of
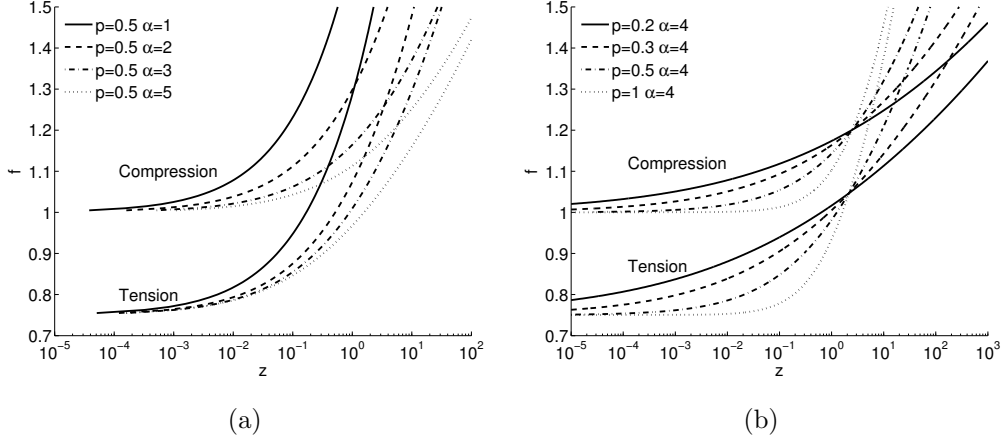
18

Figure 5: Dependency of the initial yield stress on the equivalent plastic strain rate for (a) fixed $p = 0.5$, various α and (b) various p, fixed $\alpha = 4$.

the yield stress with the strain rate is clearly captured for different values of α and p. Suitable values of α and p are then calibrated using experimental data. When the plastic strain rate tends to 0, f tends to 1 in compression and to $m = 0.75$ in tension as for the rate independent case.

3.2. Softening and failure models

In the non-local damage continuum described in Section 2, the local variables φ_s and φ_f must be defined, so that their non-local counterparts can be estimated from the implicit gradient formulations (16) and (19). As the softening and failure phenomena occur after the plasticity onset, the evolution of local variables (φ_s and φ_f) are assumed to be governed by the plastic process through the equivalent plastic strain rate. Finally, the evolution laws (17) and (20) of the softening variable D_s and of the failure variable D_f depending on their respective non-local variables and internal parameters have to be defined.

3.2.1. Softening model

In the physically-based constitutive models, as proposed by Boyce et al. (1994); Govaert et al. (2000) *e.g.*, the post-peak softening is modeled by modifying the plastic flow through the saturated evolution of an internal variable. In this work, a phenomenological-based model of the softening variable D_s is assumed.

The evolution of the local variable φ_s is directly derived from the equivalent plastic strain rate following

$$\dot{\varphi}_s = \dot{\gamma} \ \text{and} \ \varphi_s(t = 0) = 0 \,. \tag{78}$$

By the assumption that the softening variable D_s is governed by $\bar{\varphi}_s$, Eq. (17) is rewritten in a general saturation law

$$\dot{D}_s = A_s \left(D_{s\infty} - D_s \right) \dot{\chi}_s \,, \ \text{with} \ \chi_s(t) = \max \left[\chi_{s0}, \bar{\varphi}_s(\tau) \, ; \, 0 \leq \tau \leq t \, \right], \tag{79}$$

where $D_{s\infty}$ is the saturation damage value, χ_{s0} is the onset of the softening stage, and where A_s either depends on χ_s and on the internal variables, or can be considered as a constant, as suggested by Govaert et al. (2000). In this work, A_s is assumed to depend on the related non-local variable $\bar{\varphi}_s$ through the following relation

$$A_s = H_s \left(\chi_s - \chi_{s0} \right)^{\zeta_s} , \tag{80}$$

where H_s is the softening slope and where ζ_s is the softening exponent. With constant values of H_s and of ζ_s, the rate form (79) can be reformulated in an explicit form as

$$D_s = D_{s\infty} \left[1 - \exp \left(\frac{H_s}{\zeta_s + 1} \left(\chi_s - \chi_{s0} \right)^{\zeta_s + 1} \right) \right] . \tag{81}$$

The use of $\zeta_s > 0$ leads to $D_s \left(\chi_s = \chi_{s0} \right) = 0$ and $\dot{D}_s \left(\chi_s = \chi_{s0} \right) = 0$, which allows modeling the smooth post-peak softening process observed in the stress-strain curves of glassy polymers.

3.2.2. Failure model

Besides the yield criterion, the onset of the failure stage should be predicted by a failure criterion. The material strength of polymers is known to be dependent on the hydrostatic pressure as shown through various experimental results, see *e.g.* in Fiedler et al. (2001); Hine et al. (2005) for epoxy resins. The failure criterion must thus be able to capture the pressure effect. This can be achieved either by a strain-based criterion assuming the equivalent (plastic) strain at the onset of failure as a function of the stress triaxiality defined by the ratio between the pressure and the von Mises equivalent stress (Yang et al., 2012) or by a stress-based criterion related to the pressure (Melro et al., 2013). In this work, the onset of the failure stage is characterized by a pressure-dependent failure criterion based on stress invariants in order to correctly represent the pressure-sensitive failure process. This criterion is written under a general form (Melro et al., 2013) as follows

$$F_f = \Phi_f \left(\hat{\boldsymbol{\tau}}, \hat{X}_c, \hat{X}_t \right) - r \leq 0 , \tag{82}$$

where Φ_f is the failure activation function and where r is the internal variable defining the evolution of the failure surface. The activation function Φ_f is assumed to be related to the effective corotational Kirchhoff stress $\hat{\boldsymbol{\tau}}$, to $\hat{X}_c$, and to $\hat{X}_t$, which are respectively the material strengths in compression and tension, which depend on strain rates (Gerlach et al., 2008). The internal variable r has a positive time derivative and is initially equal to 0; the evolution of r obeys the Kuhn-Tucker condition

$$\dot{r} \geq 0 , F_f \leq 0 , \dot{r} F_f = 0 . \tag{83}$$

In this work, a power activation function is proposed in the form

$$\Phi_f = b_2 \left(\hat{\tau}_e \right)^{\alpha_f} - b_1 \hat{p} - b_0 , \tag{84}$$

20

where b_0, b_1, and b_2 are three failure coefficients, α_f is the failure exponent, and where

$$\hat{\tau}_e = \sqrt{\frac{3}{2}\text{dev}\,\hat{\boldsymbol{\tau}} : \text{dev}\,\hat{\boldsymbol{\tau}}} \text{ and } \hat{p} = \frac{\text{tr}\,\hat{\boldsymbol{\tau}}}{3}. \tag{85}$$

The coefficients b_0, b_1, and b_2 can be determined from the compressive and tensile material strengths, denoted by $\hat{X}_c$ and $\hat{X}_t$ respectively. Toward this end, the activation function (84) is rewritten as

$$\Phi_f = \left(\frac{\hat{\tau}_e}{\hat{\tau}_{ef}}\right)^{\alpha_f} + \frac{\hat{p}}{\hat{p}_f} - 1, \tag{86}$$

where

$$\hat{\tau}_{ef} = \hat{X}_c \left(\frac{m_f^{\alpha_f} + m_f}{m_f + 1}\right)^{\frac{1}{\alpha_f}} \text{ and} \tag{87}$$

$$\hat{p}_f = \hat{X}_c \frac{m_f^{\alpha_f} + m_f}{3\left(1 - m_f^{\alpha_f}\right)}. \tag{88}$$

In the last equations, $m_f = \hat{X}_t/\hat{X}_c > 0$ and characterizes the tension-compression failure asymmetry. In glassy polymers, the tensile failure occurs at a smaller stress compared to the compressive case, so that $m_f < 1$.

With the proposed criterion of the onset of failure, the material starts to be degraded under a pure shear stress $\hat{\tau}_{ef}$ or under an hydrostatic pressure $\hat{p}_f > 0$ as the compressive failure stress is larger than the tensile one, $m_f < 1$. This means that under a pure hydrostatic condition, the material will only fail under a positive pressure (tension state). Figure 6 represents the different failure surfaces depending on the values of the failure exponent α_f and compares them to the maximal shear stress criterion. Following the works of Melro et al. (2013); Fiedler et al. (2001), a paraboloidal failure surface, which corresponds to $\alpha_f = 2$, can be used for epoxy resins.
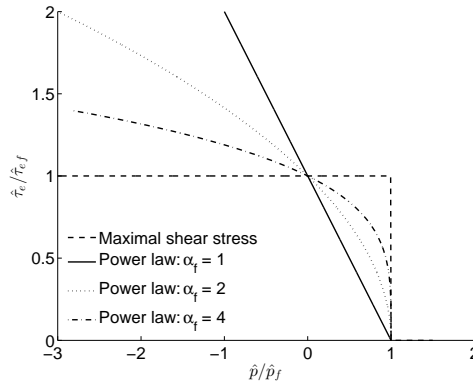

Figure 6: Dependence of the initial failure surface with the failure exponent α_f on the strain rate and comparison with the maximal shear stress criterion.

During the failure process defined by the failure condition (82), the evolution of the local variable φ_f for the failure variable is given by

$$\dot{\varphi}_f = \begin{cases} \dot{\gamma} & \text{if } \dot{r} > 0 \\ 0 & \text{if } \dot{r} = 0 \end{cases}, \tag{89}$$

with an initial condition $\varphi_f(t = 0) = 0$. The evolution of the failure variable D_f following Eq. (20) obeys the power law proposed by Brekelmans et al. (1992), which is given by

$$\dot{D}_f = H_f \left(\chi_f\right)^{\zeta_f} \left(1 - D_f\right)^{-\zeta_d} \dot{\chi}_f, \text{ with } \chi_f(t) = \max\left[\chi_{f0}, \bar{\varphi}_f(\tau) \, ; \, 0 \leq \tau \leq t\right], \tag{90}$$

where $H_f > 0$, ζ_f, and $\zeta_d > 0$ are the material parameters and where χ_{f0} is the onset of the failure stage. Assuming $\zeta_d \neq -1$, Eq. (90) can be integrated leading to an an explicit form

$$D_f = \begin{cases} 0 & \text{if } \chi_f < \chi_{f0} \\ 1 - \left[1 - H_f \frac{\zeta_d + 1}{\zeta_f + 1} \left(\chi_f^{\zeta_f + 1} - \chi_{f0}^{\zeta_f + 1}\right)\right]^{\frac{1}{\zeta_d + 1}} & \text{if } \chi_{f0} \leq \chi_f \leq \chi_{fc} \\ D_{fc} & \text{if } \chi_f > \chi_{fc} \end{cases} . \tag{91}$$

By defining the critical value χ_{fc} such that $D_f\left(\chi_{fc}\right) = D_{fc} \leq 1$, the parameter H_f can be written as

$$H_f = \frac{\zeta_f + 1}{\zeta_d + 1} \frac{1 - (1 - D_{fc})^{\zeta_d + 1}}{\chi_{fc}^{\zeta_f + 1} - \chi_{f0}^{\zeta_f + 1}} . \tag{92}$$

If $\chi_f > \chi_{fc}$, the critical state is followed by $D_f = D_{fc}$. A plateau stress is considered for this stage as the material is completely damaged.

3.3. Summary of the constitutive equations

The proposed viscoelastic-viscoplastic-damage constitutive model can be described by the following set of equations:

$$
\begin{cases}
\mathbf{F} &= \mathbf{F}^{ve} \cdot \mathbf{F}^{vp} \\[4pt]
\mathbf{E}^{ve} &= \frac{1}{2} \ln \left(\mathbf{F}^{veT} \cdot \mathbf{F}^{ve} \right) \\[4pt]
\hat{\boldsymbol{\tau}} &= \text{dev}\,\hat{\boldsymbol{\tau}} + \hat{p}\mathbf{I} = \int_{-\infty}^{t} \left[2G(t-s) : \frac{\mathrm{d}}{\mathrm{d}s}\text{dev}\,\mathbf{E}^{ve} + K(t-s)\frac{\mathrm{d}}{\mathrm{d}s}\text{tr}\,\mathbf{E}^{ve}\mathbf{I} \right]\, ds \\[4pt]
&\quad \text{Plasticity onset verification: } F \geq 0 \\[4pt]
\lambda \bar{F} &= 0\,, \lambda \geq 0 \text{ and } \bar{F} \leq 0 \\[4pt]
\mathbf{D}^{vp} &= \lambda \mathbf{Q} \\[4pt]
\dot{\mathbf{b}} &= k H_b \mathbf{D}^{vp}\,, \dot{\sigma}_c = H_c \dot{\gamma}\,, \dot{\sigma}_t = H_t \dot{\gamma} \\[4pt]
\hat{\mathbf{P}} &= \mathbf{F}^{ve} \cdot (\hat{\boldsymbol{\tau}} : \mathcal{L}) \cdot \mathbf{F}^{vp-T} \\[4pt]
\dot{D}_s &= H_s \left(\chi_s - \chi_{s0} \right)^{\zeta_s} \left(D_{s\infty} - D_s \right) \dot{\chi}_s \\[4pt]
&\quad \text{Failure onset verification: } F_f \geq 0 \\[4pt]
\dot{D}_f &= H_f \left(\chi_f \right)^{\zeta_f} \left(1 - D_f \right)^{-\zeta_d} \dot{\chi}_f \\[4pt]
\mathbf{P} &= (1 - D_s)(1 - D_f)\hat{\mathbf{P}}
\end{cases}
\tag{93}
$$

The resolution of the system of equations (93) follows the predictor-corrector scheme, see Appendix B for details.

Table 1 summarizes the material parameters entering the constitutive model. Examples of calibration tests necessary for their identification are also listed. In the viscoelastic regime, the shear and bulk moduli are expressed by Prony series of time dependent functions as detailed in Section 3.1. In the viscoplastic regime, the related constitutive parameters consist of all essential parameters of a conventional computational plasticity model (de Souza Neto et al., 2011), from which the rate effect is enhanced following a Perzyna-type flow rule with only two constants (viscosity η and rate-sensitivity exponent p). All hardening moduli (including tensile isotropic, compressive isotropic, and kinematic) are defined as functions of the equivalent plastic strain in the set of Eqs. (71-73).

Table 1 lists examples of calibration tests necessary for the identification of the material parameters of the constitutive model. Except for the yield exponent α and the failure exponent α_f, which need different tests at different values of the stress triaxiality to capture the pressure dependency, experimental tests under uniaxial loading conditions are chosen in the identification plan of the other constitutive parameters since the current constitutive model is formulated in terms of the yield and failure stresses for these loading conditions. Moreover, experimental specimens can be loaded until failure to obtain the full range of the stress-strain curve, directly resulting into the yield and failure stresses. The viscoelastic parameters can

Table 1: The material parameters of the developed constitutive model.

Stage	Description	Notations	Identification tests
Viscoelasticity	Time-dependent functions	G, K	Uniaxial tests at different strain rates
Viscoplasticity	Rate-effect constants	η, p	Uniaxial tests at different strain rates
	Yield exponent constant	α	Monotonic tests at different pressure states (different values of the stress triaxiality)
	Plastic Poisson ratio	ν_p	One uniaxial test at an arbitrary constant strain rate
	Initial yield stresses	σ_t^0, σ_c^0	One uniaxial tensile test and one uniaxial compressive test at an arbitrary constant strain rate
	Hardening functions of the equivalent plastic strain	H_t, H_c, H_b	
Saturation softening	Constants	χ_{s0}, $D_{s\infty}$, ζ_s, H_s	One uniaxial test at an arbitrary constant strain rate
Failure	Constants	χ_{f0}, ζ_d, ζ_f, H_f	One uniaxial test at an arbitrary constant strain rate
	Failure exponent constant	α_f	Monotonic tests with different pressure states (different values of the stress triaxiality)
	Material strengths as functions of strain rates	$\hat{X}_t$, $\hat{X}_c$	Uniaxial tests at different strain rates in tension and in compression

be determined from uniaxial tests at different strain rates at small strain levels, where the stress-strain relation is assumed to be viscoelastic. The parameters governing strain rate effects in the viscoplastic regime (viscosity η and rate-sensitivity exponent p) can be determined from uniaxial tests at different strain rates. The plasticity constants (ν_p, σ_t^0, and σ_c^0), hardening functions (H_t, H_c, and H_b), as well as the saturation softening constants (χ_{s0}, $D_{s\infty}$, ζ_s, and H_s) are rate-independent and can be estimated from two tests, one in compression and one in tension at an arbitrary constant strain rate by minimizing the error between the numerical prediction and the experimental response. The tensile and compressive material strengths related to the strain rates are directly obtained from performing uniaxial tensile and compression tests until reaching failure at different strain rates. As the failure behavior is assumed to be rate-independent, the related parameters (χ_{f0}, ζ_d, ζ_f, and H_f) can be estimated from one uniaxial test at an arbitrary constant strain rate. In the following sections, the current constitutive model is used to model the complex behavior of the highly cross-linked RTM6 epoxy resin at the room temperature ($\approx 20^oC$). The tested specimens fail suddenly so that the failure behavior cannot be followed. This stage is then idealized in order to model the progressive failure behavior in the context of the non-local damage continuum.

As a purely mechanical problem is formulated in this work, all material parameters are considered at a fixed temperature and isothermal processes are assumed so that the heat generation and thermal conduction are neglected. However, these effects can be taken into account in a fully thermo-mechanically-coupled simulation as considered in Anand et al. (2009); Ames et al. (2009) showing a significant influence on the stress-strain behavior. The heat generation and thermal conduction will be accounted for in a future work.

4. Experimental parameters identification

In this section, the proposed viscoelastic-viscoplastic-damage constitutive model is identified based on a wide set of experimental data of the highly cross-linked RTM6 epoxy resin at the room temperature ($\approx 20^oC$). This highly cross-linked thermoset possesses a high density of reticulation points which affect the physical properties, as discussed by Nielsen (1969); van Melick et al. (2003). Consequently, the thermo-mechanical properties of the tested epoxy resin differ from moderately cross-linked thermosets and from thermoplastics but the physical origins of the plastic flow, softening, and re-hardening can be similar (Yamini and Young, 1980). However, the highly cross-linked RTM6 epoxy resin prematurely fails under most loading conditions other than compression (Morelle et al., 2015) while moderately cross-linked polymers can still exhibit some ductility under tensile and shear loading conditions. Since the proposed constitutive model relies on the phenomenological consideration, its parameters are identified based on the experimental loading curves by curve fittings until reaching the failure onset. The failure stage is finally modeled by the progressive failure model described in Section 3.2.

4.1. Experimental tests

The uniaxial compression and tensile tests were performed until failure using a screw-driven universal testing machine. The test specimens were loaded under various constant engineering strain rates (constant cross-head displacement rates) at room temperature ($\approx 20^oC$). The results in terms of applied force versus prescribed displacement are converted to true stress- true strain curves according to the following formula

$$\sigma = \frac{F}{A_0}\left(1 + \frac{U}{L_0}\right) \text{ , and} \tag{94}$$

$$\varepsilon = \ln\left(1 + \frac{U}{L_0}\right) , \tag{95}$$

where A_0 and L_0 are the initial cross section and initial length of the specimens, σ is the true stress, ε is true strain, and where F and U are the applied force and prescribed displacement measured from experimental tests.

The uniaxial compression tests were performed on cylindrical specimens (both length and diameter equal to 12 mm) with five values of the engineering strain rate ranging from $1.4\,10^{-6}s^{-1}$ to $1.4\,10^{-1}s^{-1}$. Teflon strips were used to reduce the friction between the compressive platens and the specimens. With the use of Teflon as solid lubricant, specimen barreling can be neglected and the tests can be considered as pure uniaxial compression. The axial strain is directly obtained from the crosshead displacement corrected for the machine compliance. The uniaxial tensile tests were carried out using cylindrical dogbone specimens of gauge length 20 mm and of diameter 9 mm under a constant crosshead displacement rate of $1.1\,10^{-3}s^{-1}$. The tensile axial strain is measured using a contact extensometer in the gauge length. The use of a contact extensometer could trigger premature failure in tension of epoxy samples, and the recourse to Digital Image Correlation (DIC) or other video-based extensometry method has to be favored for strain measurement (Poulain et al., 2014). However, in the context of RTM6 resins, no shear banding nor necking could be observed under tension, mostly due to premature brittle failure before the upper yield stress. Nevertheless micro-shear banding can occur as an intrinsic material feature in RTM6, which does not necessarily translate into macro shear-banding. Besides, failure was always observed in the gauge length. As a result, the strain measurement obtained with the extensometer is thus considered valid. Tensile specimens failed in a brittle manner reaching only small strains before failure. After showing considerable plastic strains, the compressive specimens failed abruptly with the generation of a large number of fragments.

4.1.1. Uniaxial compressive tests

The average true stress- true strain curves with different engineering strain rates are shown in Fig. 7a. The multiple-stage rate-dependent stress-strain behavior is clearly observed.
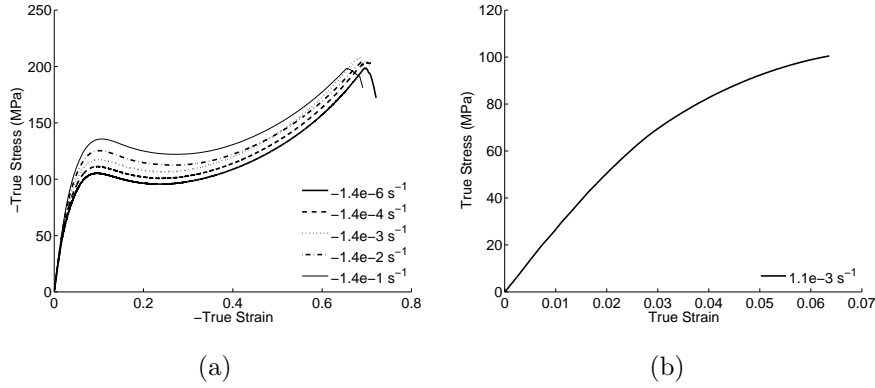
Figure 7: Experimental results with constant engineering strain rates at room temperature: (a) uniaxial compression and (b) uniaxial tensile tests.

4.1.2. Uniaxial tensile test

The obtained average stress-strain curve is shown in Fig. 7b. The brittle fracture is observed without the presence of the softening and rehardening stages.
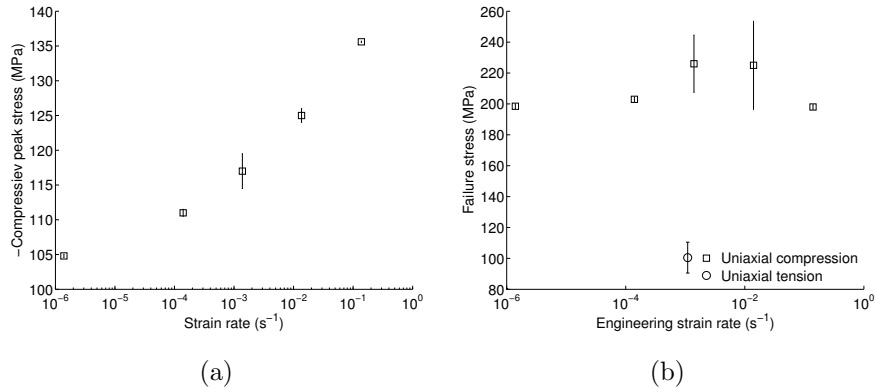
4.1.3. Peak and failure stresses

Figure 8: Compressive peak stress (a) and compressive and tensile failure stresses in terms of the strain rates (b).

The compressive peak stress and uniaxial failure stresses at various engineering strain rates are shown in Fig. 8a and b. The standard deviation is also reported. A variability is observed for both the compressive and tensile failure stresses. Fig. 8b suggests that the compressive failure stress is insensitive to strain rate. The rate insensitive assumption is also considered for the tensile failure stress. With the rate insensitive assumption, the average values of 210 MPa for the compressive failure stress and of 100 MPa for the tensile failure stress are used.

In general glassy polymers, the failure process is governed by the competition between the shear-dominated yielding mechanism in the form of strain localization bands with high plastic deformation and the

27

brittle-failure-dominated mechanism driven by the positive maximal principal stress (Estevez et al., 2000). Particularly in the highly cross-linked epoxy resin, shear yielding was observed at high temperatures while a premature brittle behavior without any progressive softening is dominant at lower temperatures (Morelle et al., 2015). Unlike the uniaxial tensile failure stress (100 MPa), which is conducted by the latter, the uniaxial compressive failure stress (210 MPa) is considered in an homogenized sense following the loading direction. On the one hand, under compression loading, although the friction between specimens and platens is minimized using lubricant films, its effect cannot be totally neglected and leads to a non-homogeneous stress state which is more-pronounced in the regions near the contact surfaces. On the other hand, the real specimens always possess some kind of defects which make the local stress state far from the pure uniaxial compression, see Chevalier et al. (2016). As a result, there exist in the specimen critical regions in which the local positive maximal principal stress and (or) the local shear stress reach their critical values yielding micro-cracks. The propagation of these initiated cracks is controlled by these true failure mechanisms resulting in the total failure of specimens under compression loading (Morelle et al., 2015). These arguments also explain the large variability on the compressive failure stresses reported in Fig. 8b. Therefore, the characterization and modeling of the true failure driving mechanisms require a micro-mechanical-based model considering the micro-structure details, as studied by Chevalier et al. (2016). In the present work, the failure process based on the compressive and tensile failure stresses is a first rudimentary approach in which the average behavior of the testing material is phenomenologically introduced by the fact that the average values over various strain rates and various specimens are used.

The constitutive parameters of the developed material model are summarized in Tab. 1. These constitutive parameters are obtained with a minimum number of experimental tests including compressive loading conditions under five engineering strain rates and a tensile loading under one engineering strain rate up to failure. For that purpose, some parameters are taken from the literature: the yield exponent $\alpha = 3.5$ is considered as this value results in a better representation of the pressure-dependency in epoxy resins as reported in Fig. 4; the plastic Poisson ratio $\nu_p = 0.3$ and the failure exponent $\alpha_f = 2$ are used as considered in Fiedler et al. (2001); Melro et al. (2013) for epoxy resins. The other parameters are identified from the performed experimental data. From the rate-dependent uniaxial compression data, the constitutive parameters governing the strain rate effects (viscoelastic parameters, viscosity parameter, and rate-sensitivity exponent) can be identified. The isotropic and kinematic hardening moduli as well as the saturation softening are assumed to be rate-independent, so they can be identified by considering two arbitrary tests with one in compression and one in tension. As the experimental specimens fail abruptly, the failure stage is therefore idealized in order to model the progressive failure behavior in the context of the non-local damage continuum.

Table 2: Viscoelastic parameters for the RTM6 epoxy resin identified from the experimental results

Viscoelastic parameters	
Number of Maxwell elements:	4
$E_\infty = 2450$ MPa	$\nu = 0.39$
$E_1 = 380$ MPa	$\tau_1 = 7000$ s
$E_2 = 190$ MPa	$\tau_2 = 70$ s
$E_3 = 95$ MPa	$\tau_3 = 0.7$ s
$E_4 = 48$ MPa	$\tau_4 = 0.07$ s

4.2. Pre-failure material parameters identification

When considering the uniaxial compression and uniaxial tensile tests, the obtained stress-strain curves are independent of the Poisson ratio, denoted by ν. In general, the Poisson ratio of polymers is shown to depend on time, stress and temperature (Tschoegl et al., 2002). Thus the Poisson ratio is not the relevant material parameter and the use of shear and bulk time functions is more appropriate to capture the multi-axial state of the material behavior (Krairi and Doghri, 2014). As only uniaxial experimental data are available, the Poisson ratio is assumed to be constant for simplicity. In this work, a Poisson ratio equal to 0.39 (Melro et al., 2013) is considered. For each spring i with $i = \infty, 1, ..., N$ in Fig. 2, the bulk modulus K_i and shear modulus G_i can be estimated from its Young's modulus E_i and the Poisson ratio ν, which is identical for all spring, as follows

$$G_i = \frac{E_i}{2(1+\nu)} \text{ and } K_i = \frac{E_i}{3(1-2\nu)} \text{ with } i = \infty, 1, ..., N. \tag{96}$$

Moreover, with the assumption that characteristic times for bulk and shear parts are identical, *i.e.* $k_i = g_i = \tau_i$ with $i = 1, ..., N$, Eqs. (45) become

$$G(t) = \frac{E(t)}{2(1+\nu)} \text{ and } K(t) = \frac{E(t)}{3(1-2\nu)} \tag{97}$$

where

$$E(t) = E_\infty + \sum_{i=1}^{N} E_i \exp\left(-\frac{t}{\tau_i}\right). \tag{98}$$

The viscoelastic behavior is characterized by the Young's moduli E_i, $i = \infty, 1, ..., N$ and retardation times τ_i, $i = 1, ..., N$. These material parameters are identified from the uniaxial tests using the simple procedure proposed by Bódai and Goda (2011). The results obtained for the RTM 6 epoxy resin are detailed in Tab. 2. A weakly viscoelastic behavior is observed as the testing temperature is far from the glass transition temperature (about 220^oC for RTM6).

The material parameters for the yield function are identified from the peak-stress values at various loading rates using Eq. (75). By assuming that the kinematic hardening stress at peak stress is negligible
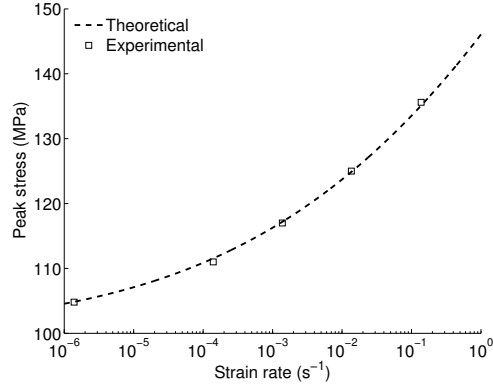
Figure 9: Dependence of the compressive peak stress on the strain rate: theoretical prediction compared to the experimental results.

Table 3: Yield parameters for the RTM6 epoxy resin identified from the experimental results

Viscoplastic parameters	
Yield exponent	$\alpha = 3.5$
Tension-compression yielding asymmetry	$m = 0.8$
Plastic Poisson ratio	$\nu_p = 0.3$
Rate sensitivity exponent	$p = 0.21$
Viscosity parameter (MPa·s)	$\eta = 3\,10^4$
Compressive peak-stress of the strain rate independent case (MPa)	$\sigma_c^p = 100$

in comparison with the isotropic hardening stress, Eq. (76) can be used with

$$f \approx \frac{|\sigma|}{\sigma_c^p} \text{ and } z \approx \frac{\eta \dot{\varepsilon}_{eng}}{\sigma_c^p}\,, \tag{99}$$

where σ_c^p corresponds to the compressive peak-stress in the rate independent case and where $\dot{\varepsilon}_{eng}$ is the absolute value of the applied engineering strain rate. The constitutive parameters reported in Tab. 3 are obtained by fitting the compression peak-stress measurements at various strain rates as shown in Fig. 9.

The pre-peak non-linearity and post-peak softening, as well as the rehardening stages are modeled using both the isotropic and kinematic hardening effects in combination with the softening model. It is assumed that the strain hardening laws (both isotropic and kinematic) and softening law are strain-rate independent and depend only on the equivalent plastic strain. Under the assumption that the isotropic hardening stress is saturated after the peak stress and that the rehardening stage arises from the kinematic hardening, as

30

Table 4: Hardening and softening parameters for the RTM6 epoxy resin identified from the experimental results

Saturation softening parameters	$\chi_{s0} = 0 \, , D_{s\infty} = 0.2 \, , \zeta_s = 1 \, , H_s = 90$
Compressive isotropic hardening model (MPa)	$\sigma_c = 48 + 55\left[1 - \exp\left(-76\gamma\right)\right]$
	$H_c = 4180 \exp\left(-76\gamma\right)$
Tensile isotropic hardening model (MPa)	$\sigma_t = m\sigma_c$
	$H_t = mH_c$
Kinematic hardening model (MPa)	$b_e = \gamma^2\left(170 - 440\gamma + 1100\gamma^2\right)$
	$H_b = \gamma\left(340 - 1320\gamma + 4400\gamma^2\right)$

assumed by Poulain et al. (2014), the hardening moduli following Eqs. (71-73) can be simplified by

$$
\begin{aligned}
H_t\left(\gamma\right) &= H_t^0 \exp\left(-K_t\gamma\right) , & (100) \\
H_c\left(\gamma\right) &= H_c^0 \exp\left(-K_c\gamma\right) , \text{ and} & (101) \\
H_b\left(\gamma\right) &= \sum_{i=0}^{M_b} \beta_i \gamma^i , & (102)
\end{aligned}
$$

where H_t^0, K_t, H_c^0, K_c, β_0, β_1,..., and β_{M_b} are material constants. Moreover, the tensile isotropic hardening stress is related to the compressive one by $\sigma_t = m\sigma_c$. By assuming that m is a constant for simplicity with its value given in Tab. 3, leading to $H_t^0 = mH_c^0$ and $K_t = K_c$.

With the hardening models (100 - 102) and the softening law (81), the numerical prediction can be obtained in terms of the hardening and softening parameters. As the analytical resolution of the system of equations (93) in the uniaxial loading conducted at a constant engineering strain rate is not easily derived, this system of equations is directly resolved in the finite element analyses using the integration algorithm described in Appendix B. For this purpose, the experimental result on the uniaxial compressive test at an engineering strain rate of $1.4\,10^{-1}\,s^{-1}$ is used. The numerical simulations are performed with a finite element model of a cylinder specimen whose dimensions are the same as in the experimental compression tests. The boundary conditions are applied to obtained the uniaxial compression state leading to the uniform resolution. This uniform resolution is independent of the mesh size and directly reflects the local resolution at a Gauss point. The obtained results in terms of the reaction force- prescribed displacement are converted into true stress-strain following Eqs. (94, 95). The numerical results are fitted to extract the parameters reported in Tab. 4.

Based on the constitutive parameters in Tabs. 2, 3 and 4, the stress-strain relationship without failure stage can be modeled. By performing finite element analyses with specimens and uniaxial loading conditions corresponding to the experimental ones, the numerical predictions are compared to the experimental results for compression in Figs. 10a, 10b and for tension in Fig. 11. Note that the failure stage has not been considered yet, the rehardening stage develops. A good agreement is obtained under various loading
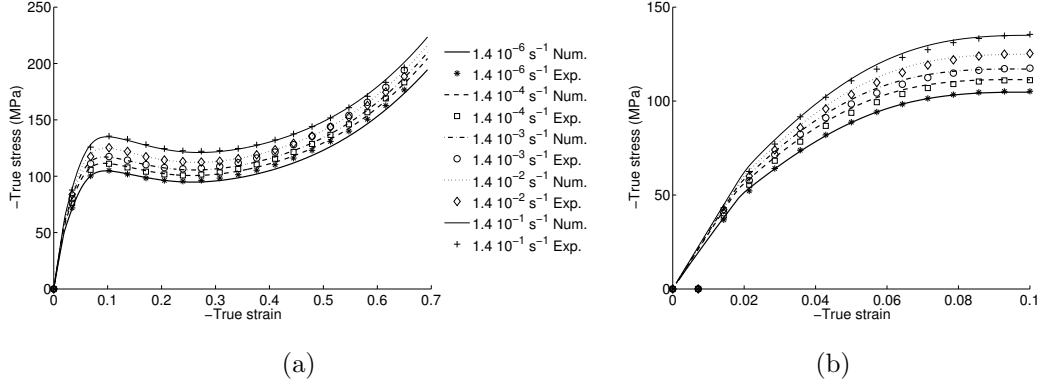
(a)   (b)

Figure 10: Model predictions compared to the experimental results for compressive stress-strain response of the RTM 6 epoxy resin at various constant engineering strain rates without considering the failure stage: (a) full strain range and (b) zoom on the pre-peak strain level.
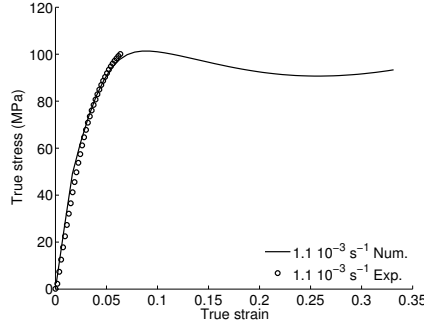

Figure 11: Model predictions compared to the experimental result for tensile stress-strain response of RTM 6 epoxy resin at a constant engineering strain rate of $1.1\,10^{-3}\ s^{-1}$ without considering the failure stage.

conditions. The material behavior will be completed with the failure stage in the next section.

4.3. Failure stage idealization

In the current work, the non-local progressive damage is considered, so that the failure stage can be idealized by a progressive damage evolution to specify the relation (91). For that purpose, the parameters characterizing the failure activation function in Eq. (84) must first be provided. As proposed by Melro et al. (2013); Fiedler et al. (2001), the failure exponent $\alpha_f = 2$, which corresponds to a paraboloid failure surface, is used in this work. The failure onset criterion is then completed with two failure stresses, defined by the absolute value of the applied stress leading to the failure state, at two distinct pressure states. As discussed above, the tensile and compressive failure stresses are assumed to be rate-independent. As the compressive failure stress is 210 MPa, one has

$$(1 - D_{s\infty})\hat{X}_c = 210 \text{ MPa or } \hat{X}_c = 262.5 \text{ MPa}. \tag{103}$$

32

As the tensile failure stress takes a value of 100 MPa and the softening variable is small in this strain range, see Tab. 4, we consider $\hat{X}_t = 100$ MPa.

When the failure criterion is met, the failure stage is characterized using a 3-dimensional finite element mesh of a cylinder of gauge length 20 mm and of diameter 9 mm as considered in Section 4.1. The uniaxial tensile loading condition (constant engineering strain rate of $1.1\,10^{-3}\,s^{-1}$) is applied. As described above, the numerical resolution of the system of equations (93) in the uniaxial loading conducted by a constant engineering strain rate is obtained by enforcing the uniform resolution using arbitrary large values for the non-local characteristic lengths. This resolution is independent of the mesh size and reflects the one at a Gauss point. The numerical predictions with different parameters of the failure softening model (91) are shown in Fig. 12a, b, and c. The tensile experimental result is also reported. The failure brittleness is more pronounced with the decrease of χ_{fc}, the increase of ζ_d as well as the increase of ζ_f.
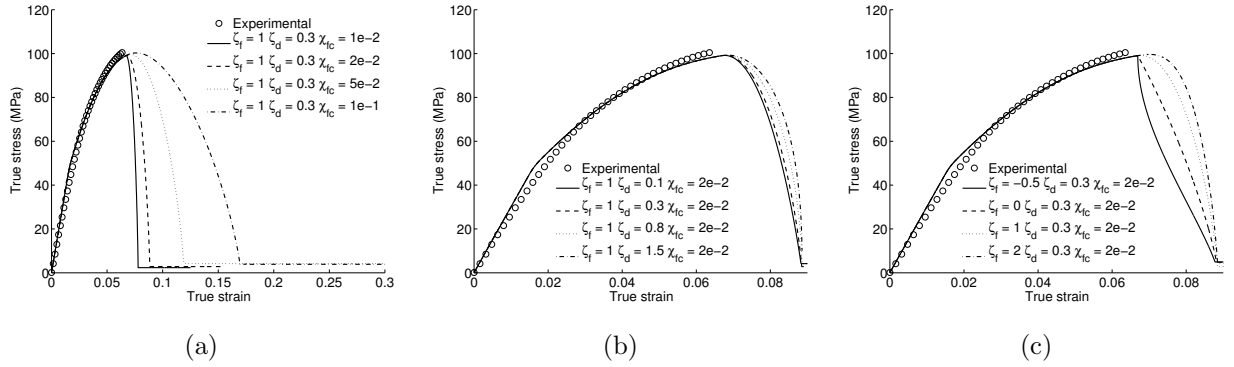

Figure 12: Influence of failure softening parameters specifying Eq. (91) on the uniaxial tensile stress-strain behavior: (a) fixed $\zeta_f = 1$, $\zeta_d = 0.3$, various χ_{fc}, (b) fixed $\zeta_f = 1$, various ζ_d, $\chi_{fc} = 2\,10^{-2}$, and (c) various ζ_f, fixed $\zeta_d = 0.3$, $\chi_{fc} = 2\,10^{-2}$. The values of $\chi_{f0} = 0$ and of $D_{fc} = 0.9$ are used for all the tests. The tensile experimental result is also reported.
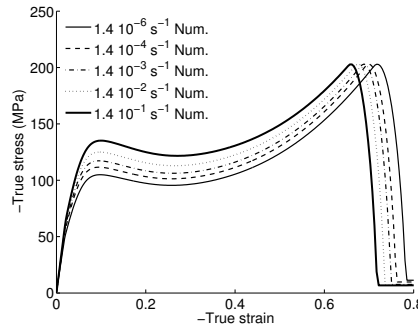

Figure 13: Model predictions of compressive stress-strain response of RTM 6 epoxy resin at various constant engineering strain rates with failure stage characterized by $\zeta_f = 1$, $\zeta_d = 0.3$, $\chi_{f0} = 0$, $\chi_{fc} = 5\,10^{-2}$, and $D_{fc} = 0.9$.

Fig. 13 depicts the numerical predictions under various engineering strain rates using the parameters reported in Tab. 5. By considering $\hat{X}_c$ independent of the strain rate, the failure stage starts at the same

33

Table 5: Progressive failure parameters for the RTM6 epoxy resin

Progressive failure parameters	
Failure exponent	$\alpha_f = 2.$
Tensile strength (MPa)	$\hat{X}_t = 100$
Compressive strength (MPa)	$\hat{X}_c = 262.5$
Failure softening parameters	$\zeta_f = 1 \, , \zeta_d = 0.3 \, , \chi_{f0} = 0 \, , \chi_{fc} = 5 \, 10^{-2}$
Critical failure damage	$D_{fc} = 0.9$

stress value. At a given strain value, a larger engineering strain rate leads to a larger stress level, so the failure stage develops earlier.

The experiment specimens failed abruptly indicating a brittle failure mechanism with a limited dissipation during cracking. In order to model the progressive failure behavior in the context of the non-local damage continuum, the failure stage is therefore idealized following Eq. (91). The proposed constitutive law is used in the context of a Newton-Raphson iterative nonlinear solver. The iterative procedure converges more difficultly with the increase of the brittleness due to the quick increase of the failure variable. In order to validate these parameters, another test with a progressive damage behavior is necessary. In this work, the failure softening parameters reported in Tab. 5 are used.
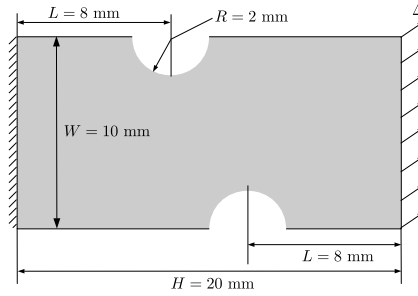
5. Mesh objectivity

Figure 14: Geometry of the double-notched specimen and boundary conditions in $x - y$ plane. The left boundary is fixed, while the right boundary is moved with prescribed displacements: $\dot{\Delta}_x = \dot{\Delta}_y = \dot{\Delta} \frac{1}{\sqrt{2}}$ and $\Delta_x = \Delta_y = \Delta \frac{1}{\sqrt{2}}$.

In this section, the 2-dimensional double-notched specimen under a quasi-static combined tensile-shear loading condition is proposed to demonstrate the mesh objectivity when using non-local implicit gradient enhanced formulation and verify the damage propagation and localization. The geometry and the boundary conditions are shown in Fig. 14. The combined loading state is obtained via prescribed displacements in both horizontal and vertical directions on the right boundary, denoted by Δ_x and Δ_y respectively. The

conditions $\Delta_x = \Delta_y = \Delta \frac{1}{\sqrt{2}}$ with displacement rates $\dot{\Delta}_x = \dot{\Delta}_y = \dot{\Delta} \frac{1}{\sqrt{2}}$ are considered. The proposed viscoelastic-viscoplastic-damage constitutive law is used with its parameters identified from Section 4, see details in Tabs. 2 - 5. The characteristics lengths $l_s^2 = l_f^2 = 2 \, \text{mm}^2$ (Geers, 1997) are used for both the softening and failure non-local implicit formulations.
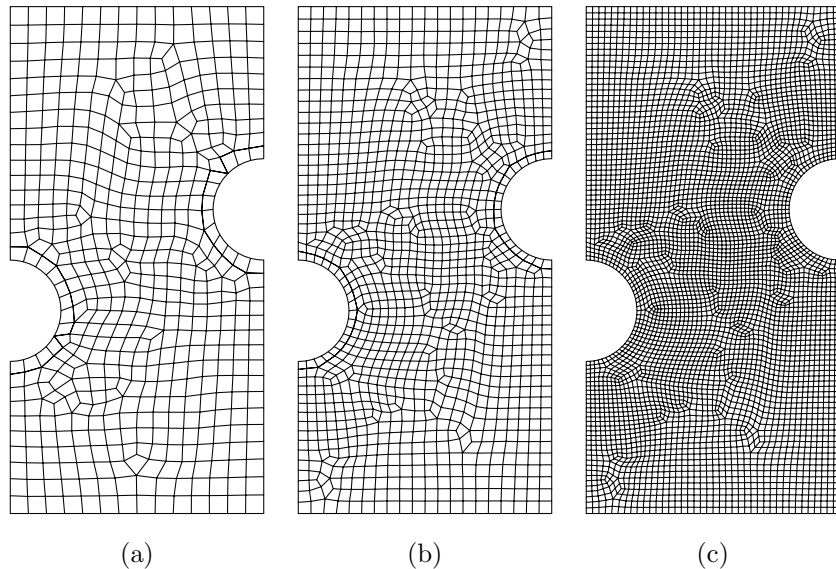

Figure 15: Meshes used in the simulations: (a) coarse mesh, (b) medium mesh, and (c) fine mesh.

The specimen is meshed using quadratic 9-node elements. Different meshes are successively considered: a coarse mesh of 530 elements (with a element size $\approx 0.3 l_f$ at the notches) as illustrated in Fig. 15a, a medium mesh of 1262 elements (with a element size $\approx 0.2 l_f$ at the notches) as illustrated in Fig. 15b, and a fine mesh of 5048 elements (with a element size $\approx 0.1 l_f$ at the notches) as illustrated in Fig. 15c. The same quadratic polynomial shape functions are used for all unknowns fields including the displacement, softening non-local variable, and failure non-local variable.
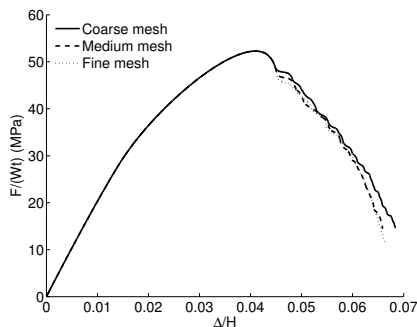

Figure 16: Comparison of the force-displacement curves obtained with different meshes under displacement rates $\dot{\Delta}_x = \dot{\Delta}_x = 10^{-3} \text{mm}/s$. In this figure, $F = \sqrt{F_x^2 + F_y^2}$, $\Delta = \sqrt{\Delta_x^2 + \Delta_y^2}$ and t is the specimen thickness.

The evolution of the reaction force $F = \sqrt{F_x^2 + F_y^2}$ with respect to the boundary displacement magnitude $\Delta = \sqrt{\Delta_x^2 + \Delta_y^2}$ is reported in Fig. 16 under a displacement rate $\dot{\Delta}_x = \dot{\Delta}_y = 10^{-3}$ mm/s for the three mesh sizes. The convergence with respect to the mesh size is clearly observed in both the pre-peak and softening stages of the overall response.
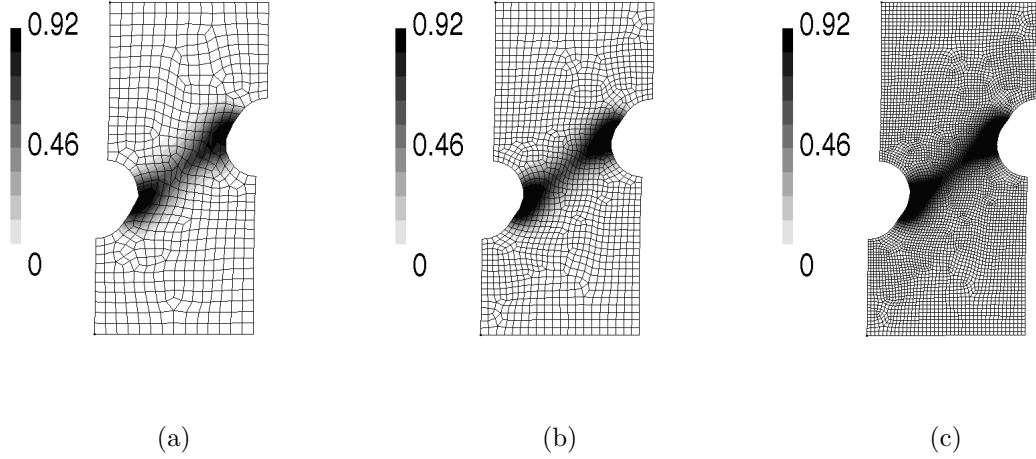

| (a) | (b) | (c) |

Figure 17: Total softening patterns with different meshes when the prescribed displacement $\Delta = 1.3$ mm: (a) coarse mesh, (b) medium mesh, and (c) fine mesh.

Figure 17 shows the distribution at the prescribed displacement $\Delta = 1.3$ mm of the total softening variable D, following the relation (9), for the three mesh sizes. The obtained results remain insensitive from the mesh size. The total damage is limited by a value of 0.92 since the softening D_s is saturated by a value of 0.2 and the failure variable D_f is limited to a value of 0.9. A larger value of D_f can be used but the numerical scheme may become unstable since the damage variable increases quickly when the damage variable is close to 1 as the property of the failure softening evolution described in Eq. (90). In order to capture these critical states, a damage-crack transition framework should be used as proposed by Wu et al. (2014).

Figure 18 shows the distributions of the softening and failure variables leading to the total softening result in Fig. 17c. The saturated value of the softening variable D_s is not reached yet; the failure occurs before the saturation of D_s, once the failure variable D_f obtains its critical value.

The force-displacement curves with different loading rates are reported in Fig. 19. The results are obtained using the medium mesh, see Fig. 15b. The ability of the proposed constitutive model to model the rate-dependent behavior is clearly observed.
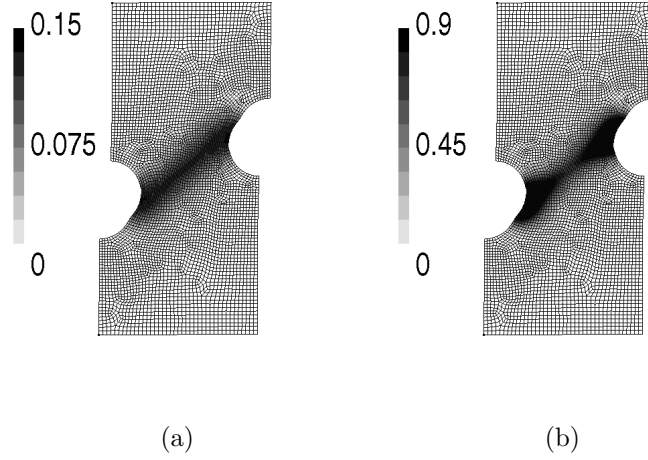
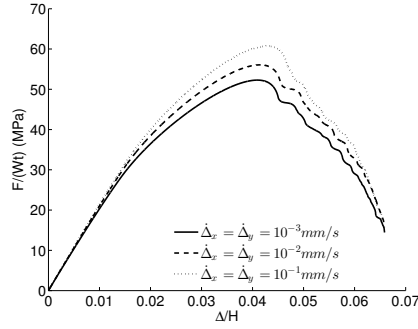Figure 18: Softening variable (a) and failure variable (b).

Figure 19: Comparison of the force-displacement curves under different displacement rates using the medium mesh.

6. Model validation

Considering the constitutive parameters reported in Tabs. 2 - 5, the current model is validated in this section against experimental results obtained at room temperature ($\approx 20^o$C).

6.1. Experimental tests

Cylindrical specimens with diameter and height both equal to 12 mm were used as considered in the uniaxial compressive tests described in Section 4. Different loading conditions were performed:

- Compression creep behavior: The specimen is first compressed under constant engineering strain rate up to a given load. Then the load is kept constant by switching from displacement control to force control. The following load levels are considered: 11 kN, 12 kN, 13 kN, and 14 kN, where this last value is close to the compressive yield peak stress. The tests were performed on the usual screw-driven universal testing machine used for compression. A solid lubrication with PTFE films was used to minimize frictional effects.

- Cyclic loading under compression: the specimen is first loaded in compression to a strain level under a constant engineering strain rate of $1.4\,10^{-3}\,s^{-1}$, then the specimen is unloaded until reaching zero stress level at the same constant engineering strain rate of $1.4\,10^{-3}\,s^{-1}$ before continuing to reach the next strain level. The solid lubrication with PTFE films was not used.

- Compression loading with friction: The compression tests were performed with and without PTFE films at two values of the engineering strain rates ($1.4\,10^{-3}\,s^{-1}$ and $1.4\,10^{-2}\,s^{-1}$) up to failure. In the case of absence of PTFE films, the friction between the platens and the specimens induces the barreling of the specimens so that the stress state cannot be considered to be homogeneous (Chevalier et al., 2016). Each test was repeated 3 times.

6.2. Finite element model

Because of the specimen symmetry, a reduced finite element model, which represents $1/8^{th}$ of the experimental specimen, consisting of 864 quadratic brick elements with 6440 finite element nodes is considered, see Fig. 20. Symmetric boundary conditions are applied in the bottom, left and front surfaces. The specimen is loaded by a moving rigid surface following the downward direction at a constant engineering strain rate. In the case of absence of PTFE films, the Coulomb friction model is adopted to account for friction at the contact surface of the top surface and the rigid surface. The friction coefficient, denoted by f, needs to be correctly determined to capture the contact conditions between the specimens and the machine platens. If $f = 0$, the uniaxial compression state is recovered because the horizontal displacement of the top surface is not constrained. The viscoelastic-viscoplastic-damage constitutive law is used with its parameters identified from Section 4, see details in Tabs. 2 - 5. The characteristics lengths $l_s^2 = l_f^2 = 2\,\text{mm}^2$ (Geers, 1997) are used for both softening and failure non-local implicit formulations.
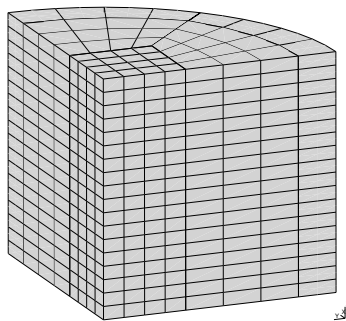

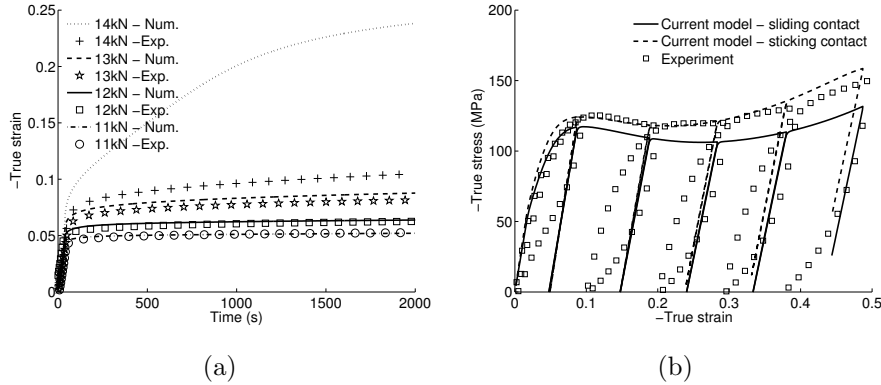Figure 20: Finite element mesh used in the finite element simulations ($1/8^{th}$ of the experimental samples).

Figure 21: Model predictions compared to the experimental data: (a) compressive creep tests and (b) compressive cyclic loading.

6.3. Results

Figure 21a shows the model predictions of the creep tests in comparison with experiments. Because of the use of PTFE films, a zero-friction contact is assumed. The current model can capture the creep behavior at low stress levels as a coupled viscoelastic-viscoplastic behavior is considered in the constitutive relation. However the use of the current model is limited at stress levels close to the peak stress. In general, most glassy polymers exhibit nonlinear viscoelastic behavior, in which the creep modulus is stress- and strain-dependent (Frank and Brockman, 2001; Abu Al-Rub et al., 2015). Moreover, when the stress level increases, the damage becomes important, so that a viscoelastic-viscoplastic constitutive model needs to be enhanced by a rate-dependent damage model to correctly capture creep behavior (Abu Al-Rub et al., 2015). With a linear viscoelastic part enhanced by the geometrical nonlinearity and coupled with viscoplastic and saturation softening parts, the current model cannot fully capture the creep behavior at stress levels close to the peak stress.

Figure 21b shows the comparisons between the results obtained by the model and by experiments under cyclic loading. Two computations were successively performed with both sticking (horizontal displacements of top surface are fully clamped) and sliding (horizontal displacements of top surface are fully free) boundary conditions. The experimental result exhibits a strong nonlinearity upon unloading (so-called Bauschinger-like effect) and hysteresis loops. During the loading phase, the experimental results are bounded by the numerical ones because of the friction effect, which becomes important as the PTFE films were not used. During unloading phase, the predicted evolution is almost linear. As only a weakly viscoelastic effect is considered and the underlying kinematic hardening part is not high enough to induce the plastic deformation during unloading phase, the current model cannot predict correctly this unloading behavior. In the literature, the nonlinearity upon unloading of glassy polymers can be modeled by considering a nonlinear viscoeslastic behavior as demonstrated by Xia et al. (2005, 2006); Colak (2005); Anand and Ames (2006). The constitutive

39

models considering the kinematic hardening can account for this nonlinear response at large strains (Anand et al., 2009; Ames et al., 2009), however they do not adequately account for this effect at small strains (Anand and Ames, 2006). Additionally, the heat generation and thermal conduction due to plastic dissipation become important at large strains and can affect both loading and unloading responses as demonstrated by Anand et al. (2009); Ames et al. (2009). A nonlinear viscoelastic model, heat generation, and thermal conduction will be considered in a future work in a fully thermo-mechanically-coupled simulation.
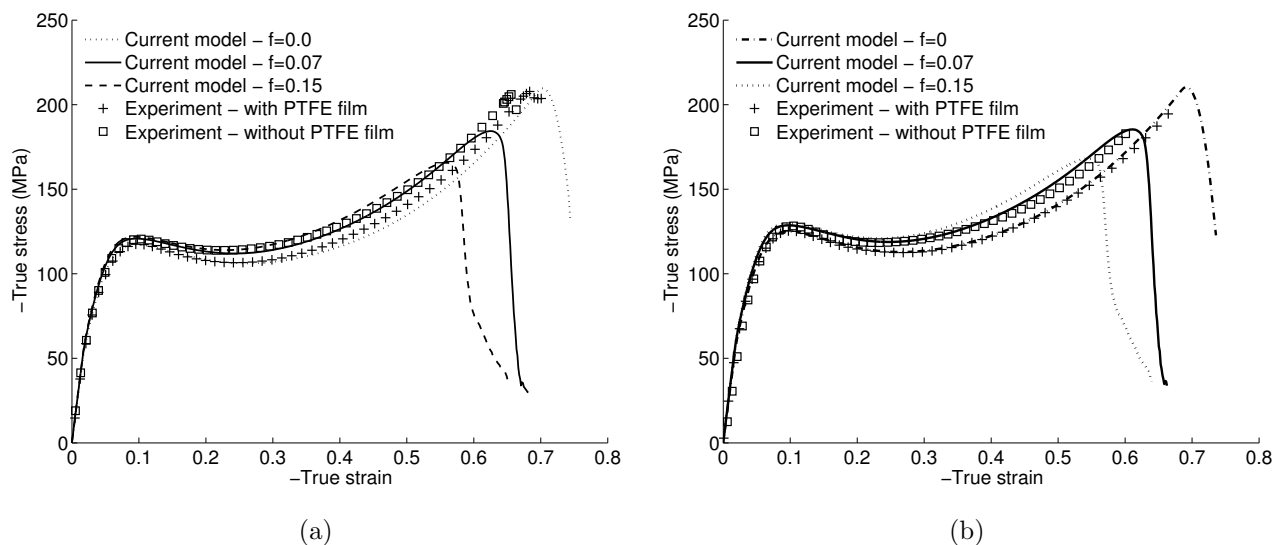

Figure 22: Model predictions compared to the experimental data: (a) compressive tests at a strain rate of $1.4 \, 10^{-3} \, s^{-1}$ and (b) compressive tests at a strain rate of $1.4 \, 10^{-2} \, s^{-1}$. Numerical results with the friction coefficient $f = 0$, 0.07, 0.15, and experimental results with and without PTFE films up to onset of failure are reported.

Figures 22a and b show the comparisons of true strain-true stress results obtained by the current model and by experiments in the case of compressive tests involving friction. Numerical simulations are performed with three friction coefficient values ($f = 0$, 0.07, and 0.15) for both engineering strain rates $1.4 \, 10^{-3} \, s^{-1}$ and $1.4 \, 10^{-2} \, s^{-1}$. The uniaxial compression tests are known to be sensitive to the friction (Fiedler et al., 2001). In the cases without PTFE films, friction is more pronounced leading to higher stress levels in the apparent stress-strain curves and earlier onset of failure. The barreling shape leads to the generation of significant stress heterogeneities, which accelerate the first crack in the specimen, explaining the earlier onset of failure (Chevalier et al., 2016). With larger values of the friction coefficient, the numerical results exhibit larger stress level and the onset of failure at a lower failure strain and at a lower failure stress in accordance with the experimental observation. This can be explained by the more pronounced barreling with the increase of the friction coefficient. The value of the friction coefficient of 0.07 provides a good agreement between the numerical and experimental results at both strain rates. A typical barreling profile when the friction coefficient is set to 0.07 at an engineering strain rate of $1.4 \, 10^{-3} \, s^{-1}$ is reported in Fig. 23b agreeing with

the corresponding experimental result illustrated in Fig. 23a.
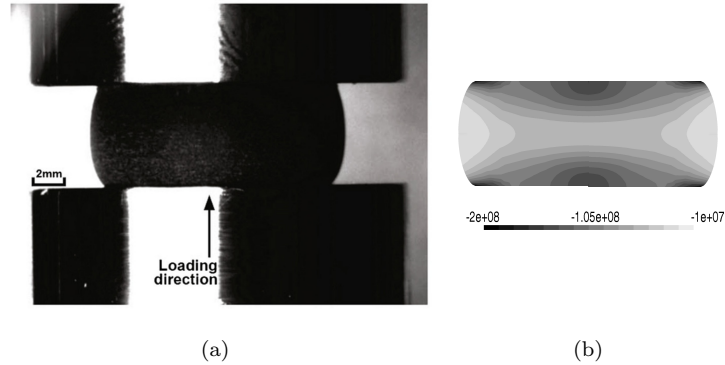

(a)   (b)

Figure 23: Barreling profile of the specimen without using the solid lubrication under compression at an engineering strain rate of $1.4\,10^{-3}\,s^{-1}$: (a) experimental result from Chevalier et al. (2016) and (b) numerical result with $f = 0.07$. The pressure distribution (in Pa) obtained from the numerical model is also reported.

7. Conclusions and perspectives

A large strain hyperelastic viscoelastic-viscoplastic-damage constitutive model has been developed with the ambition to capture the multi-stage stress-strain responses of amorphous glassy polymers. The softening and failure phenomena are modeled in the context of the non-local implicit gradient formulation in order to avoid the problem of the loss of solution uniqueness, leading to a multi-mechanism non-local damage continuum. The compression-tension asymmetry in both yielding and failure are modeled respectively by a power-enhanced yield function and by a power-enhanced failure criterion.

The proposed constitutive model is calibrated for the highly cross-linked RTM6 epoxy resin at room temperature. Through experimental results under uniaxial tensile and compression with different constant engineering strain rates, the constitutive parameters are identified. As the failure in this material occurs in a brittle way, the failure stage is idealized by a progressive damage law, which allows modeling mechanical problems in the context of the multi-mechanism damage continuum.

The mesh objectivity is clearly demonstrated by studying the behavior of the 2-dimensional double-notched specimen under a tensile/shear combined loading as the result of using non-local implicit gradient formulations to circumvent the problem of the loss of solution uniqueness.

The current model is validated through experimental results of the highly cross-linked RTM6 epoxy resin at room temperature under compressive creep loading, compressive cyclic loading, and compressive loading with friction. The current model can capture the creep behavior at low stress levels thanks to the viscoelastic constitutive part. A good agreement both in sample deformation and in overall stress-strain response is obtained in case of compressive loading with friction. However, the current model fails to

41

predict the strong hysteresis behavior upon unloading as only a weakly viscoelastic effect is considered. The viscoelastic non-linearity, the heat generation, and thermal conduction need to be considered in a future work in a fully thermo-mechanical coupled framework.

The current constitutive model is limited when the failure damage is close to 1, in that case the numerical scheme becomes unstable because of the quick increase of the damage rate. In future works, a damage-crack transition will be considered to deal with this problem, allowing to create crack when the damage reaches its critical value (smaller than 1). This constitutive law will be used to study the mechanical behavior of the fiber reinforced composites in the context of the computational micro-mechanics under different loading conditions as considered by Wu et al. (2013). The influence of the damage initialization and propagation in the matrix phase on the composite structures will be studied.

Acknowledgment

Appendix A. Weak form and finite element implementation with incremental iterative formulation

The weak form of the set of Eqs. (1, 16, 19) completed by the boundary conditions (2, 3, 22) is established using suitable weight functions defined in the $3 + N_d$ dimensional space, where N_d is the number of non-local variables (here $N_d = 2$ as D_s and D_f are considered). Considering a time step $[t_n\ t_{n+1}]$, the solution at time t_n is known and the problem is solved at time t_{n+1}. The weak form is stated as finding $(\mathbf{u}, \bar{\varphi}_k, k = 1, ..., N_d) \in [C^0(B_0)]^{3+N_d}$ such that

$$
\int_{B_0} (\mathbf{P} \otimes \boldsymbol{\nabla}_0 + \mathbf{B}_0) \cdot \delta\mathbf{u}\, d\Omega = 0\,, \text{and}
$$
$$
\int_{B_0} \left(\bar{\varphi}_k - l_k^2 \Delta_0 \bar{\varphi}_k - \varphi_k\right) \cdot \delta\bar{\varphi}_k\, d\Omega = 0 \tag{A.1}
$$
$$
\forall\, (\delta\mathbf{u}, \delta\bar{\varphi}_k, k = 1, ..., N_d) \text{ kinematically admissible}\,.
$$

Applying the divergence theorem and boundary conditions, the weak form (A.1) becomes

$$
\int_{B_0} \mathbf{P} : (\delta\mathbf{u} \otimes \boldsymbol{\nabla}_0)\, d\Omega = \int_{\partial_N B_0} \mathbf{T}_0 \cdot \delta\mathbf{u}\, d\partial\Omega + \int_{B_0} \mathbf{B}_0 \cdot \delta\mathbf{u}\, d\Omega \text{ and}
$$
$$
\int_{B_0} \left(\bar{\varphi}_k \delta\bar{\varphi}_k + l_k^2 \boldsymbol{\nabla}_0 \bar{\varphi}_k \cdot \boldsymbol{\nabla}_0 \delta\bar{\varphi}_k\right)\, d\Omega = \int_{B_0} \varphi_k \delta\bar{\varphi}_k\, d\Omega\,, \tag{A.2}
$$

with $k = 1, ..., N_d$. The displacement field and non-local variables are interpolated in each element Ω_0^e with the shape function matrices $\mathbf{N}_u$ and $\mathbf{N}_{\bar{\varphi}_k}$, such that

$$\mathbf{u} = \mathbf{N}_u \mathbf{U}, \tag{A.3}$$

$$\bar{\varphi}_k = \mathbf{N}_{\bar{\varphi}_k} \mathbf{\Phi}_k, \tag{A.4}$$

$$\delta\mathbf{u} = \mathbf{N}_u \delta\mathbf{U}, \text{ and} \tag{A.5}$$

$$\delta\bar{\varphi}_k = \mathbf{N}_{\bar{\varphi}_k} \delta\mathbf{\Phi}_k. \tag{A.6}$$

The deformation gradient and the gradient of the non-local variables are easily deduced by

$$\mathbf{F} = \mathbf{B}_u \mathbf{U}, \text{ and} \tag{A.7}$$

$$\mathbf{\nabla}_0 \bar{\varphi}_k = \mathbf{B}_{\bar{\varphi}_k} \mathbf{\Phi}_k, \tag{A.8}$$

where $\mathbf{B}_u$ and $\mathbf{B}_{\bar{\varphi}_k}$ are the matrices of the gradients of shape function $\mathbf{N}_u$ and $\mathbf{N}_{\bar{\varphi}_k}$, respectively. Using the finite element approximations (A.3-A.6), the weak form (A.2) is equivalent to the non-linear system of equations

$$\begin{bmatrix} \mathbf{F}^{int} \\ \mathbf{F}_{\bar{\varphi}_1} \\ \vdots \\ \mathbf{F}_{\bar{\varphi}_{N_d}} \end{bmatrix} - \begin{bmatrix} \mathbf{F}^{ext} \\ \mathbf{F}_{\varphi_1} \\ \vdots \\ \mathbf{F}_{\varphi_{N_d}} \end{bmatrix} = \mathbf{0}, \tag{A.9}$$

where the force vectors are given by

$$\mathbf{F}^{int} = \int_{B_0} \mathbf{B}_u^T \mathbf{P} \, d\Omega, \tag{A.10}$$

$$\mathbf{F}^{ext} = \int_{\partial_N B_0} \mathbf{N}_u^T \mathbf{T}_0 \, d\partial\Omega + \int_{B_0} \mathbf{N}_u^T \mathbf{B}_0 \, d\Omega, \tag{A.11}$$

$$\mathbf{F}_{\bar{\varphi}_k} = \int_{B_0} \left[(\mathbf{N}_{\bar{\varphi}_k})^T \mathbf{N}_{\bar{\varphi}_k} + l_k^2 (\mathbf{B}_{\bar{\varphi}_k})^T \mathbf{B}_{\bar{\varphi}_k} \right] \mathbf{\Phi}_k \, d\Omega, \text{ and} \tag{A.12}$$

$$\mathbf{F}_{\varphi_k} = \int_{B_0} (\mathbf{N}_{\bar{\varphi}_k})^T \varphi_k \, d\Omega, \tag{A.13}$$

with $k = 1, ..., N_d$. The non-linear system (A.9) is iteratively solved at iteration i for the time step $[t_n \ t_{n+1}]$ in the following matrix form

$$\begin{bmatrix} \mathbf{K}_{uu} & \mathbf{K}_{u\bar{\varphi}_1} & \mathbf{K}_{u\bar{\varphi}_2} & ... & \mathbf{K}_{u\bar{\varphi}_{N_d}} \\ \mathbf{K}_{\varphi_1 u} & \mathbf{K}_{\bar{\varphi}_1 \bar{\varphi}_1} & 0 & ... & 0 \\ \mathbf{K}_{\varphi_2 u} & 0 & \mathbf{K}_{\bar{\varphi}_2 \bar{\varphi}_2} & ... & 0 \\ \vdots & \vdots & \vdots & \ddots & \vdots \\ \mathbf{K}_{\varphi_{N_d} u} & 0 & 0 & ... & \mathbf{K}_{\bar{\varphi}_{N_d} \bar{\varphi}_{N_d}} \end{bmatrix} \begin{bmatrix} \delta\mathbf{U} \\ \delta\mathbf{\Phi}_1 \\ \delta\mathbf{\Phi}_2 \\ \vdots \\ \delta\mathbf{\Phi}_{N_d} \end{bmatrix} = \begin{bmatrix} \mathbf{F}^{ext} \\ \mathbf{F}_{\varphi_1} \\ \mathbf{F}_{\varphi_2} \\ \vdots \\ \mathbf{F}_{\varphi_{N_d}} \end{bmatrix} - \begin{bmatrix} \mathbf{F}^{int} \\ \mathbf{F}_{\bar{\varphi}_1} \\ \mathbf{F}_{\bar{\varphi}_2} \\ \vdots \\ \mathbf{F}_{\bar{\varphi}_{N_d}} \end{bmatrix}, \tag{A.14}$$

with the assumption that there is no cross term between the different non-local variables. In Eq. (A.14), the components of the global stiffness matrix are given by

$$\mathbf{K}_{uu} \quad = \quad \int_{B_0} \mathbf{B}_u^T \mathbf{C}_{uu} \mathbf{B}_u \, d\Omega \,, \tag{A.15}$$

$$\mathbf{K}_{u\bar{\varphi}_k} \quad = \quad \int_{B_0} \mathbf{B}_u^T \mathbf{C}_{u\bar{\varphi}_k} \mathbf{N}_{\bar{\varphi}_k} \, d\Omega \,, \tag{A.16}$$

$$\mathbf{K}_{\varphi_k u} \quad = \quad - \int_{B_0} \left(\mathbf{N}_{\bar{\varphi}_k} \right)^T \mathbf{S}_k \mathbf{B}_u \, d\Omega \,, \text{ and} \tag{A.17}$$

$$\mathbf{K}_{\bar{\varphi}_k \bar{\varphi}_k} \quad = \quad \int_{B_0} \left[\left(\mathbf{N}_{\bar{\varphi}_k} \right)^T \mathbf{N}_{\bar{\varphi}_k} + l_k^2 \left(\mathbf{B}_{\bar{\varphi}_k} \right)^T \mathbf{B}_{\bar{\varphi}_k} \right] \, d\Omega \text{ for } k = 1...N_d \,, \tag{A.18}$$

where

$$\mathbf{C}_{uu} \quad = \quad \frac{\partial \mathbf{P}}{\partial \mathbf{F}} = \prod_{k=1}^{N_d} (1 - D_k) \hat{\mathbb{L}} - \hat{\mathbf{P}} \otimes \sum_{k=1}^{N_d} \left[\prod_{j=1, j \neq k}^{N_d} (1 - D_j) \frac{\partial D_k}{\partial \mathbf{F}} \right] \,, \tag{A.19}$$

$$\mathbf{C}_{u\bar{\varphi}_k} \quad = \quad \frac{\partial \mathbf{P}}{\partial \bar{\varphi}_k} = -\hat{\mathbf{P}} \prod_{j=1, j \neq k}^{N_d} (1 - D_j) \frac{\partial D_k}{\partial \bar{\varphi}_k} \,, \text{ and} \tag{A.20}$$

$$\mathbf{S}_k \quad = \quad \frac{\partial \varphi_k}{\partial \mathbf{F}} \,. \tag{A.21}$$

In these last equations, $\hat{\mathbb{L}} = \frac{\partial \hat{\mathbf{P}}}{\partial \mathbf{F}}$ is the tangent operator of the undamaged constitutive law defined from Eq. (7) and given in Appendix C, $\frac{\partial D_k}{\partial \mathbf{F}}$ and $\frac{\partial D_k}{\partial \bar{\varphi}_k}$ are estimated from the damage evolution in Eqs. (17, 20), and the matrix $\mathbf{S}_k$ comes from the definition of the local variable φ_k as considered Appendix B. The derivations of $\frac{\partial D_k}{\partial \mathbf{F}}$, of $\frac{\partial D_k}{\partial \bar{\varphi}_k}$, and of $\mathbf{S}_k$ are provided in Appendix D.

Appendix B. Integration algorithm of the constitutive model

The numerical integration scheme of the current viscoelastic-viscoplastic-damage constitutive model is implemented in a typical time interval $[t_n \ t_{n+1}]$, with $t_{n+1} = t_n + \Delta t_n$. The variables in the current state at time t_{n+1}, specified without time index for simplicity, are estimated from their values from the previous state at time t_n, specified by the time index n, the current deformation gradient $\mathbf{F}$, and the current non-local variables $\bar{\varphi}_s$ and $\bar{\varphi}_f$.

Appendix B.1. Viscoelastic-viscoplastic algorithm

Following Eq. (47), the first Piola-Kirchhoff stress tensor is given at time t_{n+1} by

$$\hat{\mathbf{P}} = \mathbf{F}^{ve} \cdot \mathbf{S} \cdot \mathbf{F}^{vp-T} \,, \tag{B.1}$$

where

$$\mathbf{S} = \hat{\boldsymbol{\tau}} : \mathcal{L} \text{ with } \mathcal{L} = \frac{\partial \ln \mathbf{C}^{ve}}{\partial \mathbf{C}^{ve}} \bigg|_{\mathbf{C}^{ve}(t_{n+1})} \,. \tag{B.2}$$

44

In the numerical implementation, the logarithmic operator is approximated by

$$\ln\left(\mathbf{I} + \mathbf{A}\right) = \mathbf{A} - \frac{\mathbf{A}^2}{2} + \frac{\mathbf{A}^3}{3} - \frac{\mathbf{A}^4}{4} + ... , \tag{B.3}$$

where $\mathbf{A}$ denotes an arbitrary second-order tensor and where $\mathbf{I}$ is the identity one. Its derivative $\mathcal{L}$ is then computed from this approximation.

In order to estimate the corotational Kirchhoff stress $\hat{\boldsymbol{\tau}}$ at time t_{n+1}, the viscoelastic stress-strain relation in Eqs. (43, 44) is integrated up to the current time t_{n+1}. The deviatoric part in Eq. (43) is rewritten

$$\mathrm{dev}\,\hat{\boldsymbol{\tau}} = \int_{-\infty}^{t_{n+1}} 2G(t_{n+1} - s)\frac{\mathrm{d}}{\mathrm{d}s}\mathrm{dev}\,\mathbf{E}^{ve}(s)\,ds = 2G_\infty \mathrm{dev}\,\mathbf{E}^{ve} + \sum_{i=1}^{N} \mathbf{A}_{in+1}\,, \tag{B.4}$$

where $\mathbf{E}^{ve}$ is the current elastic strain tensor and where

$$\begin{aligned}
\mathbf{A}_{in+1} &= \int_{-\infty}^{t_{n+1}} 2G_i \exp\left(-\frac{t_{n+1} - s}{g_i}\right)\frac{\mathrm{d}}{\mathrm{d}s}\mathrm{dev}\,\mathbf{E}^{ve}(s)\,ds \\
&= \mathbf{A}_{in} \exp\left(-\frac{\Delta t_n}{g_i}\right) + \int_{t_n}^{t_{n+1}} 2G_i \exp\left(-\frac{t_{n+1} - s}{g_i}\right)\frac{\mathrm{d}}{\mathrm{d}s}\mathrm{dev}\,\mathbf{E}^{ve}(s)\,ds\,.
\end{aligned} \tag{B.5}$$

The last integral is approximated using the midpoint rule in the time interval $[t_n \; t_{n+1} = t_n + \Delta t_n]$, as

$$\begin{aligned}
&\int_{t_n}^{t_{n+1}} 2G_i \exp\left(-\frac{t_{n+1} - s}{g_i}\right)\frac{\mathrm{d}}{\mathrm{d}s}\mathrm{dev}\,\mathbf{E}^{ve}(s)\,ds \\
&\approx \left. 2G_i \exp\left(-\frac{t_{n+1} - s}{g_i}\right)\frac{\mathrm{d}}{\mathrm{d}s}\mathrm{dev}\,\mathbf{E}^{ve}(s)\right|_{s = \frac{t_{n+1} + t_n}{2}} \Delta t_n \\
&\approx 2G_i \exp\left(-\frac{\Delta t_n}{2g_i}\right)\left(\mathrm{dev}\,\mathbf{E}^{ve} - \mathrm{dev}\,\mathbf{E}_n^{ve}\right)\,.
\end{aligned} \tag{B.6}$$

Therefore, Eq. (B.5) leads to

$$\mathbf{A}_{in+1} = \mathbf{A}_{in} \exp\left(-\frac{\Delta t_n}{g_i}\right) + 2G_i \exp\left(-\frac{\Delta t_n}{2g_i}\right)\left(\mathrm{dev}\,\mathbf{E}^{ve} - \mathrm{dev}\,\mathbf{E}_n^{ve}\right)\,, \tag{B.7}$$

and Eq. (B.4) is rewritten

$$\mathrm{dev}\,\hat{\boldsymbol{\tau}} = 2G_e\mathrm{dev}\,\mathbf{E}^{ve} - 2(G_e - G_\infty)\mathrm{dev}\,\mathbf{E}_n^{ve} + \sum_{i=1}^{N}\left[\mathbf{A}_{in} \exp\left(-\frac{\Delta t_n}{g_i}\right)\right]\,, \tag{B.8}$$

where

$$G_e = G_\infty + \sum_{i=1}^{N} G_i \exp\left(-\frac{\Delta t_n}{2g_i}\right)\,. \tag{B.9}$$

Following an equivalent manipulation, the volumetric part in Eq. (44) is rewritten

$$\begin{aligned}
\hat{p} &= \int_{-\infty}^{t_{n+1}} K(t_{n+1} - s)\frac{\mathrm{d}}{\mathrm{d}s}\mathrm{tr}\,\mathbf{E}^{ve}(s)\,ds \\
&= K_\infty \mathrm{tr}\,\mathbf{E}^{ve} + \sum_{i=1}^{N} B_{in+1}\,,
\end{aligned} \tag{B.10}$$

45

where

$$B_{in+1} = B_{in} \exp\left(-\frac{\Delta t_n}{k_i}\right) + K_i \exp\left(-\frac{\Delta t_n}{2k_i}\right) \left(\operatorname{tr}\mathbf{E}^{ve} - \operatorname{tr}\mathbf{E}_n^{ve}\right) . \tag{B.11}$$

Eq. (B.10) can be finally rewritten as

$$\hat{p} = K_e \operatorname{tr}\mathbf{E}^{ve} - (K_e - K_\infty)\operatorname{tr}\mathbf{E}_n^{ve} + \sum_{i=1}^{N}\left[B_{in}\exp\left(-\frac{\Delta t_n}{k_i}\right)\right] , \tag{B.12}$$

with

$$K_e = K_\infty + \sum_{i=1}^{N} K_i \exp\left(-\frac{\Delta t_n}{2k_i}\right) . \tag{B.13}$$

The computation of the corotational Kirchhoff stress $\hat{\boldsymbol{\tau}}$, viscoelastic deformation gradient $\mathbf{F}^{ve}$, and viscoplastic deformation gradient $\mathbf{F}^{vp}$ follows a predictor-corrector scheme during the time interval $[t_n \; t_{n+1}]$. The predictor-corrector scheme is stated as follows.

Appendix B.1.1. Viscoelastic predictor

The plastic deformation tensor is initialized by its value from the previous step: $\mathbf{F}^{vppr} = \mathbf{F}_n^{vp}$. The predictor of the viscoelastic deformation gradient tensor is thus given by

$$\mathbf{F}^{vepr} = \mathbf{F} \cdot \mathbf{F}^{vppr-1} , \tag{B.14}$$

and the predictor of the viscoelastic right Cauchy strain tensor follows

$$\mathbf{C}^{vepr} = \mathbf{F}^{veprT} \cdot \mathbf{F}^{vepr} = \mathbf{F}^{vppr-T} \cdot \mathbf{F}^T \cdot \mathbf{F} \cdot \mathbf{F}^{vppr-1} = \mathbf{F}^{vppr-T} \cdot \mathbf{C} \cdot \mathbf{F}^{vppr-1} . \tag{B.15}$$

The predictors of the corotational Kirchhoff stress are deduced using Eqs. (B.8, B.12) and using $\mathbf{E}^{ve} = \mathbf{E}^{vepr} = \frac{1}{2}\ln\mathbf{C}^{vepr}$, leading to

$$\operatorname{dev}\hat{\boldsymbol{\tau}}^{pr} = 2G_e\operatorname{dev}\mathbf{E}^{vepr} - 2(G_e - G_\infty)\operatorname{dev}\mathbf{E}_n^{ve} + \sum_{i=1}^{N}\left[\mathbf{A}_i^n\exp\left(-\frac{\Delta t}{g_i}\right)\right] , \tag{B.16}$$

and

$$\hat{p}^{pr} = K_e\operatorname{tr}\mathbf{E}^{vepr} - (K_e - K_\infty)\operatorname{tr}\mathbf{E}_n^{ve} + \sum_{i=1}^{N}\left[B_i^n\exp\left(-\frac{\Delta t}{k_i}\right)\right] . \tag{B.17}$$

The yield condition (57) can then be assessed in terms of the trial value of the corotational Kirchhoff stress

$$\hat{\boldsymbol{\tau}}^{pr} = \hat{p}^{pr}\mathbf{I} + \operatorname{dev}\hat{\boldsymbol{\tau}}^{pr} , \tag{B.18}$$

where $\hat{p}^{pr}$ and $\operatorname{dev}\hat{\boldsymbol{\tau}}^{pr}$ are estimated from Eqs. (B.16, B.17) respectively. If the yield condition $F(\boldsymbol{\phi}^{pr}) \leq 0$, where $\boldsymbol{\phi}^{pr} = \hat{\boldsymbol{\tau}}^{pr} - \mathbf{b}_n$, is satisfied using this predictor, the final step is reached. Otherwise, the correction step follows.

Appendix B.1.2. Viscoplastic corrections

If the yield condition $F(\phi^{pr}) \leq 0$ is not satisfied using the predictor step, the corrector step is applied. The accumulated plastic deformation $\gamma = \gamma_n + \Delta\gamma$ is iteratively computed to satisfy the extended yield condition $\bar{F} = 0$, where $\bar{F}$ is given by Eq. (75). Integrating Eq. (29) in the time interval $[t_n \ t_{n+1}]$ using Eqs. (49, 51) leads to

$$\mathbf{F}^{vp} = \exp\left[\int_{t_n}^{t_{n+1}} \lambda(t)\mathbf{Q}(t)\,dt\right]\mathbf{F}_n^{vp}\,. \tag{B.19}$$

The flow normal $\mathbf{Q}$ is assumed to be constant in this time step and is approximated by

$$\mathbf{Q} = (1 - \zeta)\mathbf{Q}(t_n) + \zeta\mathbf{Q}(t_{n+1})\,, \tag{B.20}$$

in which ζ is a user parameter. In this work, we use $\zeta = 1$, which is known as the "radial return algorithm" (Simo and Hughes, 2006) and the notation $\mathbf{Q}(t_{n+1})$ is then replaced by $\mathbf{Q}$. Equation (B.19) thus simplifies by using Eq. (B.20) into

$$\mathbf{F}^{vp} = \exp(\Gamma\mathbf{Q})\mathbf{F}_n^{vp}\,, \tag{B.21}$$

where

$$\Gamma = \int_{t_n}^{t_{n+1}} \lambda(t)\,dt\,. \tag{B.22}$$

The elastic deformation gradient is then corrected by

$$\mathbf{F}^{ve} = \mathbf{F}\cdot\mathbf{F}^{vp-1} = \mathbf{F}\cdot\mathbf{F}_n^{vp-1}\left[\exp(\Gamma\mathbf{Q})\right]^{-1}\,, \tag{B.23}$$

and the viscoelastic right Cauchy tensor follows as

$$\mathbf{C}^{ve} = \left[\exp(\Gamma\mathbf{Q})\right]^{-T}\cdot\mathbf{C}^{vepr}\cdot\left[\exp(\Gamma\mathbf{Q})\right]^{-1}\,. \tag{B.24}$$

In terms of the viscoelastic logarithmic strain measures, Eq. (B.24) reduces to

$$\mathbf{E}^{ve} = \mathbf{E}^{vepr} - \Gamma\mathbf{Q}\,. \tag{B.25}$$

Using Eqs. (B.16, B.17), the corotational Kirchhoff stress are given by

$$\hat{\boldsymbol{\tau}} = \hat{p}\mathbf{I} + \operatorname{dev}\hat{\boldsymbol{\tau}}\,, \tag{B.26}$$

where

$$\hat{p} = \hat{p}^{pr} - K_e\Gamma\operatorname{tr}\mathbf{Q}\,, \tag{B.27}$$

$$\operatorname{dev}\hat{\boldsymbol{\tau}} = \operatorname{dev}\hat{\boldsymbol{\tau}}^{pr} - 2G_e\Gamma\operatorname{dev}\mathbf{Q}\,. \tag{B.28}$$

The backstress is estimated by integrating Eq. (67)

$$\mathbf{b} = \mathbf{b}_n + kH_b\Gamma\mathbf{Q} \,. \tag{B.29}$$

From the definition of the non-associated flow potential in Eq. (63), the flow normal $\mathbf{Q}$ is estimated using Eq. (50) by

$$\mathbf{Q} = 3\mathrm{dev}\,\boldsymbol{\phi} + \frac{2\beta}{3}\phi_p\mathbf{I} \,. \tag{B.30}$$

The equivalent plastic deformation increment $\Delta\gamma = \gamma - \gamma_n$ is estimated by integrating Eq. (65) and using Eqs. (49, 51, B.30), leading to

$$\Delta\gamma = k\Gamma\sqrt{\mathbf{Q}:\mathbf{Q}} = k\Gamma\sqrt{6\phi_e{}^2 + \frac{4}{3}\beta^2\phi_p{}^2} \,. \tag{B.31}$$

Combining Eqs. (B.27 - B.30) leads to

$$\phi_p = \frac{\phi_p^{pr}}{v} \,, \tag{B.32}$$

$$\mathrm{dev}\,\boldsymbol{\phi} = \frac{\mathrm{dev}\,\boldsymbol{\phi}^{pr}}{u} \,, \text{ and} \tag{B.33}$$

$$\phi_e = \frac{\phi_e^{pr}}{u} \,, \tag{B.34}$$

where

$$u = 1 + 6\tilde{G}\Gamma \,, v = 1 + 2\beta\tilde{K}\Gamma \,, \tilde{G} = G_e + \frac{k}{2}H_b \,, \text{ and } \tilde{K} = K_e + \frac{k}{3}H_b \,. \tag{B.35}$$

Finally, using these results, Eq. (B.31) leads to

$$\Delta\gamma = k\Gamma A \,, \tag{B.36}$$

where

$$A = \sqrt{6\frac{(\phi_e^{pr})^2}{u^2} + \frac{4\beta^2}{3}\frac{(\phi_p^{pr})^2}{v^2}} \,. \tag{B.37}$$

The extended yield condition (75) can be rewritten using the trial values and the flow parameter Γ as

$$\bar{F} = a_2\left(\frac{\phi_e^{pr}}{u}\right)^\alpha - a_1\frac{\phi_p^{pr}}{v} - a_0 - \left(\eta\frac{\Gamma}{\Delta t}\right)^p = 0 \,, \tag{B.38}$$

where the viscoplastic flow parameter λ is approximated from Eq. (B.22) by

$$\lambda = \frac{\Gamma}{\Delta t} \,. \tag{B.39}$$

Since Γ is the only unknown of Eq. (B.38), this equation can be iteratively solved by the Newton-Raphson procedure. For that purpose, the derivative of $\bar{F}$ with respect to Γ is required:

$$\frac{\mathrm{d}\bar{F}}{\mathrm{d}\Gamma} = \left[H_2\left(\frac{\phi_e^{pr}}{u}\right)^\alpha - H_1\frac{\phi_p^{pr}}{v} - H_0\right]\frac{\partial\Delta\gamma}{\partial\Gamma} + \frac{\partial\bar{F}}{\partial\Gamma} \,, \tag{B.40}$$

with

$$H_2 \quad = \quad \frac{\partial a_2}{\partial \Delta \gamma} = -\frac{\alpha}{\sigma_c^{\alpha+1}} H_c , \tag{B.41}$$

$$H_1 \quad = \quad \frac{\partial a_1}{\partial \Delta \gamma} = \frac{3}{\sigma_c} \left[\frac{\alpha m^{\alpha-1}}{m+1} - \frac{m^\alpha - 1}{(m+1)^2} \right] \frac{H_t \sigma_c - H_c \sigma_t}{\sigma_c^2} - 3 \frac{m^\alpha - 1}{m+1} \frac{H_c}{\sigma_c^2} , \tag{B.42}$$

$$H_0 \quad = \quad \frac{\partial a_0}{\partial \Delta \gamma} = \frac{(\alpha m^{\alpha-1} + 1)(m+1) - m^\alpha - m}{(m+1)^2} \frac{H_t \sigma_c - H_c \sigma_t}{\sigma_c^2} , \tag{B.43}$$

$$\frac{\partial \bar{F}}{\partial \Gamma} \quad = \quad -a_2 \left(\frac{\phi_e^{pr}}{u} \right)^\alpha \frac{\alpha 6 \tilde{G}}{u} + a_1 \frac{\phi_p^{pr}}{v} \frac{2\beta \tilde{K}}{v} - \left(\frac{\eta}{\Delta t} \right)^p p \Gamma^{p-1} , \tag{B.44}$$

$$\frac{\partial \Delta \gamma}{\partial \Gamma} \quad = \quad k \left(A + \gamma \frac{\partial A}{\partial \Gamma} \right) , \text{ and} \tag{B.45}$$

$$\frac{\partial A}{\partial \Gamma} \quad = \quad -\frac{1}{2A} \left[\frac{72 \tilde{G}(\phi_e^{pr})^2}{u^3} + \frac{16 \tilde{K} \beta^3 (\phi_p^{pr})^2}{3v^3} \right] . \tag{B.46}$$

Appendix B.1.3. Final step

The effective first Piola-Kirchhoff stress $\hat{\mathbf{P}}$ is eventually estimated using Eq. (B.1). The computation of the effective tangent operator $\frac{\partial \hat{\mathbf{P}}}{\partial \mathbf{F}}$ is detailed in Appendix C.

Appendix B.2. Softening and failure variables

Because of the non-local formulation, the resolution of the effective stress $\hat{\mathbf{P}}$ is locally uncoupled from the evolution of the softening variable D_s and of the failure variable D_f. The coupling is achieved through the finite element resolution, see Appendix A.

The historical non-local variable χ_s is given by

$$\begin{cases} \chi_s = \chi_{sn} & \text{if } \bar{\varphi}_s \leq \chi_{sn} \\ \chi_s = \bar{\varphi}_s & \text{if } \bar{\varphi}_s > \chi_{sn} \end{cases} , \tag{B.47}$$

where the non-local value $\bar{\varphi}_s$ follows the finite element resolution. The evolution of the softening variable D_s at time t_{n+1} is directly estimated using Eq. (81).

From the stress resolution of the viscoelastic-viscoplastic constitutive law, the prediction of the failure criterion in Eq. (82) is estimated by

$$F_f^{pr} = \Phi_f \left(\hat{\boldsymbol{\tau}}, \hat{X}_c, \hat{X}_t \right) - r_n \leq 0 , \tag{B.48}$$

leading to the estimation of the internal variable r at time t_{n+1} using Eq. (83) as

$$r = \begin{cases} r_n & \text{if } F_f^{pr} \leq 0 \\ \Phi_f \left(\hat{\boldsymbol{\tau}}, \hat{X}_c, \hat{X}_t \right) & \text{if } F_f^{pr} > 0 \end{cases} , \tag{B.49}$$

in order to satisfy $F_f = 0$. Using Eq. (89), the value of the local variable φ^f is then given by

$$\varphi_f = \begin{cases} \varphi_{fn} & \text{if } r = r_n \\ \varphi_{fn} + \Delta\gamma & \text{if } r > r_n \end{cases}, \tag{B.50}$$

where $\Delta\gamma$ is given in Eq. (B.31). The historical non-local variable χ_f is given by

$$\begin{cases} \chi_f = \chi_{fn} & \text{if } \bar{\varphi}_f \leq \chi_{fn} \\ \chi_f = \bar{\varphi}_f & \text{if } \bar{\varphi}_f > \chi_{fn} \end{cases}, \tag{B.51}$$

where the non-local value $\bar{\varphi}_f$ follows the finite element resolution. The evolution of the failure variable D_f at the time t_{n+1} is directly estimated using Eq. (91).

The derivatives of local variables, of the softening variable, and of failure variable required for the iterative procedure of the finite element resolution are detailed in Appendix D.

Appendix C. Effective material tangent operator

From Eq. (B.1), the effective tangent operator is estimated by the relation

$$\hat{\mathbb{L}} = \frac{\partial \hat{\mathbf{P}}}{\partial \mathbf{F}} = \frac{\partial \mathbf{F}^{ve}}{\partial \mathbf{F}} \, {}^2\!\cdot (\mathbf{S} \cdot \mathbf{F}^{vp}) + \mathbf{F}^{ve} \, {}^{.1}\frac{\partial \mathbf{S}}{\partial \mathbf{F}} \, {}^2\!\cdot \mathbf{F}^{vp} + (\mathbf{F}^{ve} \cdot \mathbf{S}) \cdot \frac{\partial \mathbf{F}^{vp-1}}{\partial \mathbf{F}}, \tag{C.1}$$

where ${}^i\!\cdot$ $(\cdot^i)$ is the ith left (right) dot product operator of two tensors considering i^{th} index of the left (right) tensor.

The relation $\mathbf{F}^{ve} = \mathbf{F} \cdot \mathbf{F}^{vp-1}$ leads to

$$\frac{\partial \mathbf{F}^{ve}}{\partial \mathbf{F}} = (\mathbf{I} \otimes \mathbf{I}) \, {}^2\!\cdot \mathbf{F}^{vp-1} + \mathbf{F} \cdot \frac{\partial \mathbf{F}^{vp-1}}{\partial \mathbf{F}}. \tag{C.2}$$

From $\mathbf{F}^{vp} \cdot \mathbf{F}^{vp-1} = \mathbf{I}$, one has

$$\frac{\partial \mathbf{F}^{vp-1}}{\partial \mathbf{F}} = -\mathbf{F}^{vp-1} \cdot \frac{\partial \mathbf{F}^{vp}}{\partial \mathbf{F}} \, {}^2\!\cdot \mathbf{F}^{vp-1}. \tag{C.3}$$

To compute the tangent operator $\hat{\mathbb{L}}$, the values of $\frac{\partial \mathbf{S}}{\partial \mathbf{F}}$ and $\frac{\partial \mathbf{F}^{vp}}{\partial \mathbf{F}}$ need to be estimated. The definition of the right Cauchy strain tensor (25) yields

$$\frac{\partial \bullet}{\partial \mathbf{F}} = \frac{\partial \bullet}{\partial \mathbf{C}} : \frac{\partial \mathbf{C}}{\partial \mathbf{F}}, \tag{C.4}$$

where $\bullet$ represents an arbitrary tensor field. Using Eq. (B.15) leads to

$$\frac{\partial \bullet}{\partial \mathbf{C}} = \mathbf{F}^{vppr-1} \cdot \frac{\partial \bullet}{\partial \mathbf{C}^{vepr}} \cdot \mathbf{F}^{vppr-T}. \tag{C.5}$$

Therefore, $\frac{\partial \mathbf{S}}{\partial \mathbf{C}^{vepr}}$ and $\frac{\partial \mathbf{F}^{vp}}{\partial \mathbf{C}^{vepr}}$ have to be estimated. Eq. (B.21) leads to

$$\frac{\partial \mathbf{F}^{vp}}{\partial \mathbf{C}^{vepr}} = \left[\mathcal{E} : \left(\mathbf{Q} \otimes \frac{\partial \Gamma}{\partial \mathbf{C}^{vepr}} + \Gamma \frac{\partial \text{dev}\,\mathbf{Q}}{\partial \mathbf{C}^{vepr}} + \frac{\Gamma}{3}\mathbf{I} \otimes \frac{\partial \text{tr}\,\mathbf{Q}}{\partial \mathbf{C}^{vepr}} \right) \right] \, {}^2\!\cdot \mathbf{F}_n^{vp}, \tag{C.6}$$

where

$$\mathcal{E} = \frac{\partial \exp \mathbf{A}}{\partial \mathbf{A}}\bigg|_{\Gamma \mathbf{Q}} . \tag{C.7}$$

Equation (B.2) leads to

$$\frac{\partial \mathbf{S}}{\partial \mathbf{C}^{vepr}} = \frac{\partial \mathcal{L}}{\partial \mathbf{C}^{vepr}}^{3,4} : \hat{\boldsymbol{\tau}} + \mathcal{L} : \frac{\partial \hat{\boldsymbol{\tau}}}{\partial \mathbf{C}^{vepr}} , \tag{C.8}$$

where

$$\frac{\partial \hat{\boldsymbol{\tau}}}{\partial \mathbf{C}^{vepr}} = \mathbf{I} \otimes \frac{\partial \hat{p}}{\partial \mathbf{C}^{vepr}} + \frac{\partial \operatorname{dev} \hat{\boldsymbol{\tau}}}{\partial \mathbf{C}^{vepr}} . \tag{C.9}$$

Using Eq. (B.27), one has

$$\frac{\partial \hat{p}}{\partial \mathbf{C}^{vepr}} = \frac{\partial \hat{p}^{pr}}{\partial \mathbf{C}^{vepr}} - K_e \Gamma \frac{\partial \operatorname{tr} \mathbf{Q}}{\partial \mathbf{C}^{vepr}} - K_e \frac{\partial \Gamma}{\partial \mathbf{C}^{vepr}} \operatorname{tr} \mathbf{Q} . \tag{C.10}$$

Equation (B.17) leads to

$$\frac{\partial \hat{p}^{pr}}{\partial \mathbf{C}^{vepr}} = \frac{\partial \hat{p}^{pr}}{\partial \mathbf{E}^{vepr}} : \frac{\partial \mathbf{E}^{vepr}}{\partial \mathbf{C}^{vepr}} = \frac{K_e}{2} \mathbf{I} : \mathcal{L}^{pr} , \tag{C.11}$$

where

$$\mathcal{L}^{pr} = \frac{\partial \ln \mathbf{C}^{ve}}{\partial \mathbf{C}^{ve}}\bigg|_{\mathbf{C}^{vepr}} . \tag{C.12}$$

Using Eq. (B.28), one has

$$\frac{\partial \operatorname{dev} \hat{\boldsymbol{\tau}}}{\partial \mathbf{C}^{vepr}} = \frac{\partial \operatorname{dev} \hat{\boldsymbol{\tau}}^{pr}}{\partial \mathbf{C}^{vepr}} - 2G_e \Gamma \frac{\partial \operatorname{dev} \mathbf{Q}}{\partial \mathbf{C}^{vepr}} - 2G_e \operatorname{dev} \mathbf{Q} \otimes \frac{\partial \Gamma}{\partial \mathbf{C}^{vepr}} . \tag{C.13}$$

Equation (B.16) leads to

$$\frac{\partial \operatorname{dev} \hat{\boldsymbol{\tau}}^{pr}}{\partial \mathbf{C}^{vepr}} = \frac{\partial \operatorname{dev} \hat{\boldsymbol{\tau}}^{pr}}{\partial \mathbf{E}^{vepr}} : \frac{\partial \mathbf{E}^{vepr}}{\partial \mathbf{C}^{vepr}} = G_e \left(\mathcal{I} - \frac{1}{3} \mathbf{I} \otimes \mathbf{I} \right) : \mathcal{L}^{pr} . \tag{C.14}$$

Finally, it is necessary to compute $\frac{\partial \Gamma}{\partial \mathbf{C}^{vepr}}$, $\frac{\partial \operatorname{dev} \mathbf{Q}}{\partial \mathbf{C}^{vepr}}$ and $\frac{\partial \operatorname{tr} \mathbf{Q}}{\partial \mathbf{C}^{vepr}}$. Eqs. (B.30, B.32) lead to

$$\frac{\partial \operatorname{tr} \mathbf{Q}}{\partial \mathbf{C}^{vepr}} = \frac{2\beta}{v} \frac{\partial \hat{p}^{pr}}{\partial \mathbf{C}^{vepr}} - \frac{4\tilde{K}\beta^2 \phi_p^{pr}}{v^2} \frac{\partial \Gamma}{\partial \mathbf{C}^{vepr}} , \tag{C.15}$$

and Eqs. (B.30, B.33) lead to

$$\frac{\partial \operatorname{dev} \mathbf{Q}}{\partial \mathbf{C}^{vepr}} = \frac{3}{u} \frac{\partial \operatorname{dev} \hat{\boldsymbol{\tau}}^{pr}}{\partial \mathbf{C}^{vepr}} - \frac{18\tilde{G}}{u^2} \operatorname{dev} \boldsymbol{\phi}^{pr} \otimes \frac{\partial \Gamma}{\partial \mathbf{C}^{vepr}} . \tag{C.16}$$

The value of $\frac{\partial \Gamma}{\partial \mathbf{C}^{vepr}}$ is estimated from the consistency condition of the yield condition, *i.e.*

$$\mathrm{d}\bar{F}(\mathbf{C}^{vepr}, \Delta\gamma, \Gamma) = 0 , \tag{C.17}$$

which is detailed by

$$\frac{\partial \bar{F}}{\partial \mathbf{C}^{vepr}} + \left[H_2 \left(\frac{\phi_e^{pr}}{u} \right)^\alpha - H_1 \frac{\phi_p^{pr}}{v} - H_0 \right] \frac{\partial \Delta\gamma}{\partial \mathbf{C}^{vepr}} + \left(\frac{\partial F}{\partial \Gamma} + \frac{\partial \bar{F}}{\partial \Delta\gamma} \frac{\partial \Delta\gamma}{\partial \Gamma} \right) \frac{\partial \Gamma}{\partial \mathbf{C}^{vepr}} = 0 , \tag{C.18}$$

51

where

$$\frac{\partial \bar{F}}{\partial \mathbf{C}^{vepr}} = \frac{a_2}{u^\alpha}\frac{\alpha}{2}(\phi_e^{pr})^{\alpha-2}3\mathrm{dev}\,\boldsymbol{\phi}^{pr} : \frac{\partial \mathrm{dev}\,\hat{\boldsymbol{\tau}}^{pr}}{\partial \mathbf{C}^{vepr}} - \frac{a_1}{v}\frac{\partial \hat{p}^{pr}}{\partial \mathbf{C}^{vepr}}\,, \tag{C.19}$$

$$\frac{\partial \Delta\gamma}{\partial \mathbf{C}^{vepr}} = k\Gamma\frac{\partial A}{\partial \mathbf{C}^{vepr}}\,, \tag{C.20}$$

$$\frac{\partial A}{\partial \mathbf{C}^{vepr}} = \frac{1}{2A}\left(\frac{18}{u^2}\mathrm{dev}\,\boldsymbol{\phi}^{pr} : \frac{\partial \mathrm{dev}\,\hat{\boldsymbol{\tau}}^{pr}}{\partial \mathbf{C}^{vepr}} + \frac{8\beta^2}{3v^2}\phi_p^{pr}\frac{\partial \hat{p}^{pr}}{\partial \mathbf{C}^{vepr}}\right)\,. \tag{C.21}$$

Finally, one has

$$\frac{\partial \Gamma}{\partial \mathbf{C}^{vepr}} = -\frac{\frac{\partial \bar{F}}{\partial \mathbf{C}^{vepr}} + \frac{\partial \bar{F}}{\partial \Delta\gamma}\frac{\partial \Delta\gamma}{\partial \mathbf{C}^{vepr}}}{\frac{\partial \bar{F}}{\partial \Gamma} + \frac{\partial \bar{F}}{\partial \Delta\gamma}\frac{\partial \Delta\gamma}{\partial \Gamma}}\,. \tag{C.22}$$

The value of $\frac{\partial \gamma}{\partial \mathbf{F}}$ is estimated from $\frac{\partial \gamma}{\partial \mathbf{C}^{vepr}}$, which is given by

$$\frac{\partial \gamma}{\partial \mathbf{C}^{vepr}} = k\Gamma\frac{\partial A}{\partial \mathbf{C}^{vepr}} + k\left(A + \Gamma\frac{\partial A}{\partial \Gamma}\right)\frac{\partial \Gamma}{\partial \mathbf{C}^{vepr}}\,. \tag{C.23}$$

Appendix D. Derivatives of local variables and of the softening variables

From the definition of the local variables φ_s, φ_f, their derivatives with respect to $\mathbf{F}$ are required to evaluate Eq. (A.21). Following Eq. (78), one has

$$\mathbf{S}_s = \frac{\partial \gamma}{\partial \mathbf{F}}\,. \tag{D.1}$$

Equation (89) leads to

$$\mathbf{S}_f = \begin{cases} 0 & \text{if } r = r_n \\ \frac{\partial \gamma}{\partial \mathbf{F}} & \text{if } r > r_n \end{cases}\,. \tag{D.2}$$

Using Eq. (79), the derivatives resulting from the softening law required to estimate the relations (A.19, A.20) are given by

$$\frac{\partial D_s}{\partial \mathbf{F}} = \mathbf{0} \quad \text{and} \tag{D.3}$$

$$\frac{\partial D_s}{\partial \bar{\varphi}^s} = \begin{cases} 0 & \text{if } \chi_s \leq \chi_{sn} \\ (D_{s\infty} - D_s)H_s\,(\chi_s)^{\zeta_s} & \text{if } \chi_s > \chi_{sn} \end{cases}\,. \tag{D.4}$$

Using Eq. (90), the required derivatives from the failure softening law for Eqs. (A.19, A.20) are given by

$$\frac{\partial D_f}{\partial \mathbf{F}} = \mathbf{0}\,, \quad \text{and} \tag{D.5}$$

$$\frac{\partial D_f}{\partial \bar{\varphi}_f} = \begin{cases} 0 & \text{if } \chi_f \leq \chi_{fn} \\ H_f\,(\chi_f)^{\zeta_f}\,(1 - D_f)^{-\zeta_d} & \text{if } \chi_{fn} < \chi_f \leq \chi_{fc} \\ 0 & \text{if } \chi_f > \chi_{fc} \end{cases}\,. \tag{D.6}$$

References

Abu Al-Rub, R. K., Tehrani, A. H., Darabi, M. K., 2015. Application of a large deformation nonlinear-viscoelastic viscoplastic viscodamage constitutive model to polymers and their composites. International Journal of Damage Mechanics 24 (2), 198–244.
URL http://ijd.sagepub.com/content/24/2/198.abstract

Ames, N. M., Srivastava, V., Chester, S. A., Anand, L., 2009. A thermo-mechanically coupled theory for large deformations of amorphous polymers. part ii: Applications. International Journal of Plasticity 25 (8), 1495 – 1539.
URL http://www.sciencedirect.com/science/article/pii/S074964190800171X

Anand, L., Ames, N., 2006. On modeling the micro-indentation response of an amorphous polymer. International Journal of Plasticity 22 (6), 1123 – 1170.
URL http://www.sciencedirect.com/science/article/pii/S0749641905001415

Anand, L., Ames, N. M., Srivastava, V., Chester, S. A., 2009. A thermo-mechanically coupled theory for large deformations of amorphous polymers. part i: Formulation. International Journal of Plasticity 25 (8), 1474 – 1494.
URL http://www.sciencedirect.com/science/article/pii/S0749641908001708

Arruda, E. M., Boyce, M. C., Jayachandran, R., 1995. Effects of strain rate, temperature and thermomechanical coupling on the finite strain deformation of glassy polymers. Mechanics of Materials 19 (23), 193 – 212.
URL http://www.sciencedirect.com/science/article/pii/016766369400034E

Bazant, Z. P., Jirásek, M., 2002. Nonlocal integral formulations of plasticity and damage: survey of progress. Journal of Engineering Mechanics 128 (11), 1119–1149.

Bigoni, D., Piccolroaz, A., 2004. Yield criteria for quasibrittle and frictional materials. International Journal of Solids and Structures 41 (1112), 2855 – 2878.
URL http://www.sciencedirect.com/science/article/pii/S0020768303007273

Bódai, G., Goda, T., 2011. A new, tensile test-based parameter identification method for large-strain generalized maxwell-model. Acta Polytechnica Hungarica 8 (5), 89–108.

Bodner, S., Partom, Y., 1975. Constitutive equations for elastic-viscoplastic strain-hardening materials. Journal of Applied Mechanics 42 (2), 385–389.

Boyce, M. C., Arruda, E. M., Jayachandran, R., 1994. The large strain compression, tension, and simple shear of polycarbonate. Polymer Engineering & Science 34 (9), 716–725.
URL http://dx.doi.org/10.1002/pen.760340904

Boyce, M. C., Parks, D. M., Argon, A. S., Sep. 1988. Large inelastic deformation of glassy polymers. part I: rate dependent constitutive model. Mechanics of Materials 7 (1), 15–33.
URL http://www.sciencedirect.com/science/article/pii/0167663688900038

Brekelmans, W., Schreurs, P., de Vree, J., 1992. Continuum damage mechanics for softening of brittle materials. Acta Mechanica 93 (1-4), 133–143.
URL http://dx.doi.org/10.1007/BF01182579

Buckley, C., Harding, J., Hou, J., Ruiz, C., Trojanowski, A., 2001. Deformation of thermosetting resins at impact rates of strain. part i: Experimental study. Journal of the Mechanics and Physics of Solids 49 (7), 1517 – 1538.
URL http://www.sciencedirect.com/science/article/pii/S0022509600000855

Buhan, M. d., Frey, P., 2011. A generalized model of non-linear viscoelasticity: numerical issues and applications. International Journal for Numerical Methods in Engineering 86 (13), 1544–1557.
URL http://dx.doi.org/10.1002/nme.3115

Canal, L. P., Segurado, J., LLorca, J., 2009. Failure surface of epoxy-modified fiber-reinforced composites under transverse

tension and out-of-plane shear. International Journal of Solids and Structures 46 (1112), 2265 – 2274.

URL http://www.sciencedirect.com/science/article/pii/S0020768309000341

Chen, W., Lu, F., Cheng, M., 2002. Tension and compression tests of two polymers under quasi-static and dynamic loading. Polymer Testing 21 (2), 113 – 121.

URL http://www.sciencedirect.com/science/article/pii/S0142941801000551

Chevalier, J., Morelle, X., Bailly, C., Camanho, P., Pardoen, T., Lani, F., 2016. Micro-mechanics based pressure dependent failure model for highly cross-linked epoxy resins. Engineering Fracture Mechanics 158, 1 – 12.

URL http://www.sciencedirect.com/science/article/pii/S0013794416300571

Chowdhury, K., Benzerga, A., Talreja, R., 2008a. An analysis of impact-induced deformation and fracture modes in amorphous glassy polymers. Engineering Fracture Mechanics 75 (11), 3328 – 3342, local Approach to Fracture (19862006): Selected papers from the 9th European Mechanics of Materials Conference.

URL http://www.sciencedirect.com/science/article/pii/S0013794407003451

Chowdhury, K., Talreja, R., Benzerga, A., 2008b. Effects of manufacturing-induced voids on local failure in polymer-based composites. Journal of Engineering Materials and Technology, Transactions of the ASME 130 (2), 0210101 – 0210109.

Colak, O. U., 2005. Modeling deformation behavior of polymers with viscoplasticity theory based on overstress. International Journal of Plasticity 21 (1), 145 – 160.

URL http://www.sciencedirect.com/science/article/pii/S074964190400049X

Cuitino, A., Ortiz, M., 1992. A material-independent method for extending stress update algorithms from small-strain plasticity to finite plasticity with multiplicative kinematics. Engineering Computations 9 (4), 437–451.

de Souza Neto, E. A., Peric, D., Owen, D. R. J., 2011. Computational methods for plasticity: theory and applications. John Wiley & Sons.

Engelen, R. A., Geers, M. G., Baaijens, F. P., 2003. Nonlocal implicit gradient-enhanced elasto-plasticity for the modelling of softening behaviour. International Journal of Plasticity 19 (4), 403 – 433.

URL http://www.sciencedirect.com/science/article/pii/S0749641901000420

Estevez, R., Tijssens, M., der Giessen, E. V., 2000. Modeling of the competition between shear yielding and crazing in glassy polymers. Journal of the Mechanics and Physics of Solids 48 (12), 2585 – 2617.

URL http://www.sciencedirect.com/science/article/pii/S0022509600000168

Eterovic, A. L., Bathe, K.-J., 1990. A hyperelastic-based large strain elasto-plastic constitutive formulation with combined isotropic-kinematic hardening using the logarithmic stress and strain measures. International Journal for Numerical Methods in Engineering 30 (6), 1099–1114.

URL http://dx.doi.org/10.1002/nme.1620300602

Fiedler, B., Hojo, M., Ochiai, S., Schulte, K., Ando, M., 2001. Failure behavior of an epoxy matrix under different kinds of static loading. Composites Science and Technology 61 (11), 1615 – 1624.

URL http://www.sciencedirect.com/science/article/pii/S0266353801000574

Frank, G. J., Brockman, R. A., 2001. A viscoelastic-viscoplastic constitutive model for glassy polymers. International Journal of Solids and Structures 38 (30-31), 5149 – 5164.

URL http://www.sciencedirect.com/science/article/pii/S0020768300003395

Geers, M., Borst, R., Brekelmans, W., Peerlings, R., 1999. Validation and internal length scale determination for a gradient damage model: application to short glass-fibre-reinforced polypropylene. International Journal of Solids and Structures 36 (17), 2557 – 2583.

URL http://www.sciencedirect.com/science/article/pii/S0020768398001231

Geers, M. G. D., 1997. Experimental analysis and computational modelling of damage and fracture. Ph.D. thesis, Technische Universiteit Eindhoven.

Gerlach, R., Siviour, C. R., Petrinic, N., Wiegand, J., 2008. Experimental characterisation and constitutive modelling of rtm-6 resin under impact loading. Polymer 49 (11), 2728 – 2737.

URL http://www.sciencedirect.com/science/article/pii/S0032386108003406

Govaert, L., Timmermans, P., Brekelmans, W., 2000. The influence of intrinsic strain softening on strain localization in polycarbonate: modeling and experimental validation. Journal of Engineering Materials and Technology 122 (2), 177–185.

Haj-Ali, R. M., Muliana, A. H., 2004. Numerical finite element formulation of the schapery non-linear viscoelastic material model. International Journal for Numerical Methods in Engineering 59 (1), 25–45.

URL http://dx.doi.org/10.1002/nme.861

Hine, P., Duckett, R., Kaddour, A., Hinton, M., Wells, G., Feb. 2005. The effect of hydrostatic pressure on the mechanical properties of glass fibre/epoxy unidirectional composites. Composites Part A: Applied Science and Manufacturing 36 (2), 279–289.

URL http://www.sciencedirect.com/science/article/pii/S1359835X04001526

Kachanov, L., 2013. Introduction to continuum damage mechanics. Vol. 10. Springer Science & Business Media.

Kim, J.-S., Muliana, A. H., 2010. A combined viscoelasticviscoplastic behavior of particle reinforced composites. International Journal of Solids and Structures 47 (5), 580 – 594.

URL http://www.sciencedirect.com/science/article/pii/S0020768309004120

Krairi, A., Doghri, I., 2014. A thermodynamically-based constitutive model for thermoplastic polymers coupling viscoelasticity, viscoplasticity and ductile damage. International Journal of Plasticity 60 (0), 163 – 181.

URL http://www.sciencedirect.com/science/article/pii/S074964191400093X

Krempl, E., McMahon, J., Yao, D., 1986. Viscoplasticity based on overstress with a differential growth law for the equilibrium stress. Mechanics of Materials 5 (1), 35 – 48.

URL http://www.sciencedirect.com/science/article/pii/0167663686900141

Lemaitre, J., 1985. Coupled elasto-plasticity and damage constitutive equations. Computer Methods in Applied Mechanics and Engineering 51 (13), 31 – 49.

URL http://www.sciencedirect.com/science/article/pii/004578258590026X

Lemaitre, J., Chaboche, J.-L., 1994. Mechanics of solid materials. Cambridge university press.

Lesser, A. J., Kody, R. S., 1997. A generalized model for the yield behavior of epoxy networks in multiaxial stress states. Journal of Polymer Science Part B: Polymer Physics 35 (10), 1611–1619.

URL http://dx.doi.org/10.1002/(SICI)1099-0488(19970730)35:10<1611::AID-POLB13>3.0.CO;2-D

Melro, A., Camanho, P., Pires, F. A., Pinho, S., 2013. Micromechanical analysis of polymer composites reinforced by unidirectional fibres: Part i constitutive modelling. International Journal of Solids and Structures 50 (1112), 1897 – 1905.

URL http://www.sciencedirect.com/science/article/pii/S0020768313000747

Miled, B., Doghri, I., Delannay, L., 2011. Coupled viscoelasticviscoplastic modeling of homogeneous and isotropic polymers: Numerical algorithm and analytical solutions. Computer Methods in Applied Mechanics and Engineering 200 (4748), 3381 – 3394.

URL http://www.sciencedirect.com/science/article/pii/S0045782511002702

Moran, B., Ortiz, M., Shih, C. F., 1990. Formulation of implicit finite element methods for multiplicative finite deformation plasticity. International Journal for Numerical Methods in Engineering 29 (3), 483–514.

URL http://dx.doi.org/10.1002/nme.1620290304

Morelle, X., 2015. Mechanical characterization and physics-based modeling of highly-crosslinked epoxy resin. Ph.D. thesis, Université catholique de Louvain.

Morelle, X. P., Chevalier, J., Bailly, C., Pardoen, T., Lani, F., 2015. Mechanical characterization and modeling of the deformation and failure of the highly cross-linked rtm6 epoxy resin. Submitted to International Journal of Plasticity.

Mulliken, A., Boyce, M., 2006. Mechanics of the rate-dependent elasticplastic deformation of glassy polymers from low to high strain rates. International Journal of Solids and Structures 43 (5), 1331 – 1356.

URL http://www.sciencedirect.com/science/article/pii/S0020768305002313

Nielsen, L. E., 1969. Cross-linking effect on physical properties of polymers. Journal of Macromolecular Science, Part C 3 (1), 69–103.

URL http://dx.doi.org/10.1080/15583726908545897

Peerlings, R., Geers, M., de Borst, R., Brekelmans, W., 2001. A critical comparison of nonlocal and gradient-enhanced softening continua. International Journal of Solids and Structures 38 (4445), 7723 – 7746.

URL http://www.sciencedirect.com/science/article/pii/S0020768301000877

Peerlings, R. H. J., De Borst, R., Brekelmans, W. A. M., De Vree, J. H. P., 1996. Gradient enhanced damage for quasi-brittle materials. International Journal for Numerical Methods in Engineering 39 (19), 3391–3403.

URL http://www.scopus.com/inward/record.url?eid=2-s2.0-0030267284&partnerID=tZOtx3y1

Perzyna, P., 1971. Thermodynamic theory of viscoplasticity. Vol. 11 of Advances in Applied Mechanics. Elsevier, pp. 313 – 354.

URL http://www.sciencedirect.com/science/article/pii/S0065215608703454

Poulain, X., Benzerga, A., Goldberg, R., 2014. Finite-strain elasto-viscoplastic behavior of an epoxy resin: Experiments and modeling in the glassy regime. International Journal of Plasticity 62, 138 – 161.

URL http://www.sciencedirect.com/science/article/pii/S0749641914001351

Reese, S., Govindjee, S., 1998. A theory of finite viscoelasticity and numerical aspects. International Journal of Solids and Structures 35 (2627), 3455 – 3482.

URL http://www.sciencedirect.com/science/article/pii/S0020768397002175

Sauer, J. a., Mar. 1977. Deformation, yield and fracture of polymers at high pressure. Polymer Engineering and Science 17 (3), 150–164.

URL http://doi.wiley.com/10.1002/pen.760170304

Schiessel, H., Metzler, R., Blumen, A., Nonnenmacher, T. F., 1995. Generalized viscoelastic models: their fractional equations with solutions. Journal of Physics A: Mathematical and General 28 (23), 6567.

URL http://stacks.iop.org/0305-4470/28/i=23/a=012

Selke, A. E., 2016. Variational models of thermo-viscoelastic damage: applications to polymer behavior and coupling with the thick level set approach to non-local damage. Ph.D. thesis, Ecole Centrale de Nantes.

Shu, J. Y., Barlow, C. Y., 2000. Strain gradient effects on microscopic strain field in a metal matrix composite. International Journal of Plasticity 16 (5), 563 – 591.

URL http://www.sciencedirect.com/science/article/pii/S0749641999000881

Simo, J., 1987. On a fully three-dimensional finite-strain viscoelastic damage model: Formulation and computational aspects. Computer Methods in Applied Mechanics and Engineering 60 (2), 153 – 173.

URL http://www.sciencedirect.com/science/article/pii/0045782587901071

Simo, J. C., Hughes, T. J., 2006. Computational inelasticity. Vol. 7. Springer Science & Business Media.

Stölken, J., Evans, A., 1998. A microbend test method for measuring the plasticity length scale. Acta Materialia 46 (14), 5109 – 5115.

URL http://www.sciencedirect.com/science/article/pii/S1359645498001530

Tervoort, T., Smit, R., Brekelmans, W., Govaert, L., 1997. A constitutive equation for the elasto-viscoplastic deformation of glassy polymers. Mechanics of Time-Dependent Materials 1 (3), 269–291.

Tschoegl, N., Knauss, W., Emri, I., 2002. Poisson's ratio in linear viscoelasticity a critical review. Mechanics of Time-Dependent Materials 6 (1), 3–51.

URL http://dx.doi.org/10.1023/A%3A1014411503170

Van Der Sluis, O., Schreurs, P., Meijer, H., 2001. Homogenisation of structured elastoviscoplastic solids at finite strains. Mechanics of Materials 33 (9), 499–522.

van Melick, H., Govaert, L., Meijer, H., 2003. On the origin of strain hardening in glassy polymers. Polymer 44 (8), 2493 – 2502.
URL `http://www.sciencedirect.com/science/article/pii/S0032386103001125`

Vogler, M., Rolfes, R., Camanho, P., 2013. Modeling the inelastic deformation and fracture of polymer composites part i: Plasticity model. Mechanics of Materials 59, 50 – 64.
URL `http://www.sciencedirect.com/science/article/pii/S016766361200213X`

Wu, L., Becker, G., Noels, L., 2014. Elastic damage to crack transition in a coupled non-local implicit discontinuous galerkin/extrinsic cohesive law framework. Computer Methods in Applied Mechanics and Engineering 279, 379 – 409.
URL `http://www.sciencedirect.com/science/article/pii/S0045782514002175`

Wu, L., Tjahjanto, D., Becker, G., Makradi, A., Jérusalem, A., Noels, L., 2013. A micromeso-model of intra-laminar fracture in fiber-reinforced composites based on a discontinuous galerkin/cohesive zone method. Engineering Fracture Mechanics 104, 162 – 183.
URL `http://www.sciencedirect.com/science/article/pii/S0013794413001252`

Wu, P., van der Giessen, E., 1995. On neck propagation in amorphous glassy polymers under plane strain tension. International Journal of Plasticity 11 (3), 211 – 235.
URL `http://www.sciencedirect.com/science/article/pii/0749641994000433`

Xia, Z., Shen, X., Ellyin, F., 2005. Cyclic deformation behavior of an epoxy polymer. part ii: Predictions of viscoelastic constitutive models. Polymer Engineering & Science 45 (1), 103–113.
URL `http://dx.doi.org/10.1002/pen.20235`

Xia, Z., Shen, X., Ellyin, F., 2006. An assessment of nonlinearly viscoelastic constitutive models for cyclic loading: The effect of a general loading/unloading rule. Mechanics of Time-Dependent Materials 9 (4), 79–98.
URL `http://dx.doi.org/10.1007/s11043-006-9004-3`

Yamini, S., Young, R., 1980. The mechanical properties of epoxy resins. Journal of Materials Science 15 (7), 1814–1822.
URL `http://dx.doi.org/10.1007/BF00550602`

Yang, L., Yan, Y., Liu, Y., Ran, Z., 2012. Microscopic failure mechanisms of fiber-reinforced polymer composites under transverse tension and compression. Composites Science and Technology 72 (15), 1818 – 1825.
URL `http://www.sciencedirect.com/science/article/pii/S0266353812002928`

Zaïri, F., Naït-Abdelaziz, M., Gloaguen, J., Lefebvre, J., 2008. Modelling of the elasto-viscoplastic damage behaviour of glassy polymers. International Journal of Plasticity 24 (6), 945 – 965.
URL `http://www.sciencedirect.com/science/article/pii/S074964190700112X`

Zhang, C., Moore, I. D., 1997. Nonlinear mechanical response of high density polyethylene. part ii: Uniaxial constitutive modeling. Polymer Engineering & Science 37 (2), 414–420.
URL `http://dx.doi.org/10.1002/pen.11684`